



Spatially resolved direct method metallicity in a high-redshift analogue local galaxy: temperature structure impact on metallicity gradients

Alex J. Cameron^{1,2,★}, Tiantian Yuan^{2,3}, Michele Trenti^{1,2}, David C. Nicholls^{2,4} and Lisa J. Kewley^{2,4}

¹*School of Physics, The University of Melbourne, Parkville, VIC 3010, Australia*

²*ARC Centre of Excellence for All-Sky Astrophysics in 3 Dimensions (ASTRO 3D), Australia*

³*Centre for Astrophysics and Supercomputing, Swinburne University of Technology, Hawthorn, VIC 3122, Australia*

⁴*Research School of Astronomy and Astrophysics, The Australian National University, Cotter Road, Weston, ACT 2611, Australia*

Accepted 2020 November 26. Received 2020 October 29; in original form 2020 August 24

ABSTRACT

We investigate how H II region temperature structure assumptions affect ‘direct-method’ spatially resolved metallicity observations using multispecies auroral lines in a galaxy from the SAMI Galaxy Survey. SAMI609396B, at redshift $z = 0.018$, is a low-mass galaxy in a minor merger with intense star formation, analogous to conditions at high redshifts. We use three methods to derive direct metallicities and compare with strong-line diagnostics. The spatial metallicity trends show significant differences among the three direct methods. Our first method is based on the commonly used electron temperature $T_e([\text{O III}])$ from the $[\text{O III}]\lambda 4363$ auroral line and a traditional $T_e([\text{O II}]) - T_e([\text{O III}])$ calibration. The second method applies a recent empirical correction to the O^+ abundance from the $[\text{O III}]/[\text{O II}]$ strong-line ratio. The third method infers the $T_e([\text{O II}])$ from the $[\text{S II}]\lambda\lambda 4069, 76$ auroral lines. The first method favours a positive metallicity gradient along SAMI609396B, whereas the second and third methods yield flattened gradients. Strong-line diagnostics produce mostly flat gradients, albeit with unquantified contamination from shocked regions. We conclude that overlooked assumptions about the internal temperature structure of H II regions in the direct method can lead to large discrepancies in metallicity gradient studies. Our detailed analysis of SAMI609396B underlines that high-accuracy metallicity gradient measurements require a wide array of emission lines and improved spatial resolutions in order to properly constrain excitation sources, physical conditions, and temperature structures of the emitting gas. Integral-field spectroscopic studies with future facilities such as *JWST*/NIRSpec and ground-based ELTs will be crucial in minimizing systematic effects on measured gradients in distant galaxies.

Key words: ISM: abundances – galaxies: abundances – galaxies: fundamental parameters – galaxies: ISM.

1 INTRODUCTION

Abundances of heavy elements (metallicities) in the interstellar medium (ISM) of galaxies are enriched by stellar nucleosynthesis and trace star formation histories and gas-flow processes that ultimately shape the galaxy population. In particular, the spatial distribution of metallicity offers a powerful probe on the role of mergers, outflows, gas mixing, and gas accretion in transforming galaxies (e.g. Edmunds & Greenhow 1995; Kewley et al. 2010; Torrey et al. 2012; Magrini et al. 2016; Finlator 2017; Ma et al. 2017; Bresolin 2019; Tissera et al. 2019; Hemler et al. 2020). Spatial distributions of metals are often summarized as radial abundance gradients and azimuthal variations (e.g. Searle 1971; Vila-Costas & Edmunds 1992; Li, Bresolin & Kennicutt 2013; Ho et al. 2015, 2019), with both negative and flat metallicity gradients widely observed in the Milky Way and other local galaxies (e.g. Deharveng et al. 2000; Bresolin, Garnett & Kennicutt 2004; Berg et al. 2013, 2020).

Spatially resolved studies of galaxies are now far more accessible compared to a decade ago, thanks to the advent of integral-field unit (IFU) spectroscopy. Multiplexed IFU surveys (e.g. CALIFA,

Sánchez et al. 2012; SAMI, Bryant et al. 2015; MaNGA, Bundy et al. 2015) have afforded large samples of gradient measurements in the local Universe. Studies find a dependence on stellar mass: low-mass galaxies ($\sim 10^9 M_\odot$) show almost flat gradients, with negative gradients steepening to high masses (Belfiore et al. 2017; Poetrodjojo et al. 2018). Spatially resolved measurements become more challenging at high redshift and observations show a substantial amount of scatter (Yuan et al. 2011; Jones et al. 2013; Leethochawalit et al. 2016; Carton et al. 2018; Curti et al. 2020b; Wang et al. 2020). One major caveat in using this broad range of observations to develop a coherent model of galaxy evolution is that different measurement techniques are often in disagreement.

A number of observational methods exist for determining the oxygen abundance (metallicity hereafter) of the ISM in galaxies from emission line spectroscopy (see Kewley, Nicholls & Sutherland 2019; Maiolino & Mannucci 2019 for recent reviews). However, different techniques often show large offsets up to 0.7 dex (e.g. Kewley & Ellison 2008; Peimbert, Peimbert & Delgado-Inglada 2017). This stark disagreement between different metallicity measurement techniques presents an ongoing challenge for studying chemical evolution of galaxies.

Emission line strengths in the photoionized nebulae around hot O- and B-type stars (H II regions) are sensitive to electron temperature

* E-mail: alexc@student.unimelb.edu.au

(T_e), in addition to ionic abundances, ionization parameter, and ISM pressure. Thus, a desirable approach to metallicity measurement is to use ratios of auroral emission lines and corresponding strong nebular emission lines to explicitly determine T_e , and subsequently metallicity (Direct Method; e.g. see Pérez-Montero 2017 for an overview). This ‘direct method’ is traditionally considered the gold standard in abundance determination (e.g. Maiolino & Mannucci 2019), and underpins the calibration of many alternative techniques (e.g. Pettini & Pagel 2004; Curti et al. 2020a). However, one major practical issue with the direct method is that the faintness of the optical auroral lines severely limits its application. An alternative T_e -based method outlined by Jones et al. (2020) determines oxygen abundance based instead on far-infrared oxygen lines ([O III] 52 μm or [O III] 88 μm). This is expected to be favourable beyond $z \gtrsim 5$ where these far-IR features can be observed with millimeter instruments such as *ALMA*, but is difficult to apply at lower redshifts.

Due to the faintness of auroral lines required for the direct method, strong-line methods are widely adopted in observations. Strong-line methods use ratios of the brightest rest-frame ultraviolet and optical emission lines to empirically determine the metallicity with calibrations based on either direct-method observations (e.g. Pettini & Pagel 2004; Pilyugin & Thuan 2005; Curti et al. 2020a) or stellar population synthesis and photoionization models (e.g. Kewley & Dopita 2002; Kobulnicky & Kewley 2004; Dopita et al. 2016). Strong-line methods vastly expand the redshift and mass range of galaxies for which metallicities can be derived. However, it has been widely observed that metallicities measured with different methods often disagree (e.g. Kewley & Ellison 2008; Moustakas et al. 2010; Morales-Luis et al. 2014). In particular, theoretical methods, are reliant on simple geometries, such as spherical or plane-parallel, and assume a constant temperature, constant density, or a constant pressure.

Despite the baseline role of the direct method, it does have limitations beyond practical detection-rate issues (Nicholls, Kewley & Sutherland 2020; Yates et al. 2020). H II regions are complex structures and summarizing their conditions with integrated measurements of emission line ratios carries many assumptions. For example, H II regions are known to have internal temperature variations (Peimbert 1967; Kewley et al. 2019). An observed emission line ratio samples the luminosity-weighted average conditions of the emitting nebulae (Nicholls et al. 2020). The direct method is best applied by constructing a multizone temperature model using auroral lines from multiple ionic species (e.g. Pérez-Montero 2017; Berg et al. 2020). Commonly used auroral lines include those from O^{2+} , O^+ , N^+ , or S^{2+} ions.¹ This allows internal temperature gradients to be sampled since ions with differing ionization energies preferentially sample different subregions of the nebulae.

However, measuring auroral lines from multiple species in observations presents a difficult practical challenge. Even detection of a single auroral line, commonly [O III] $\lambda 4363$, is generally considered a favourable outcome. But since the [O III] $\lambda 4363$ line is only produced in the hottest regions of a nebula, a resulting T_e -derived metallicity may be a lower limit to the true metallicity if there is a temperature gradient (Kewley et al. 2019). To overcome the lack of direct constraints on the multizone temperature structure, abundance measurements are often made adopting empirical relations between temperatures from different ions. For example, the [O II] temperature ($T_e(\text{[O II]})$) is indirectly inferred from the [O III]

temperature ($T_e(\text{[O III]})$; based on [O III] $\lambda 4363$) using the $T_e(\text{[O II]}) - T_e(\text{[O III]})$ relation (e.g. Izotov et al. 2006; López-Sánchez et al. 2012; Pérez-Montero 2017). Recently, Yates et al. (2020) show that at low O^{2+}/O^+ , this approach can lead to large deficits in the measured O^+ abundance, causing total oxygen abundances to be underestimated by up to ~ 0.6 dex.

Studying metallicity in spatially resolved detail exacerbates the practical limitations of the direct method. Indeed, direct method metallicities have been mapped only for the Milky Way and small samples of large nearby spiral galaxies (Deharveng et al. 2000; Bresolin et al. 2004; Berg et al. 2013, 2015, 2020; Li et al. 2013; Croxall et al. 2015, 2016; Ho et al. 2019), exploring only a very narrow subset of the galaxy population. Here we leverage public release IFU data from the SAMI Galaxy Survey to expand spatially resolved direct method metallicity measurements to a new parameter space. From a search of auroral lines in SAMI Data Release 2 data cubes, we identify one particularly strong candidate: SAMI609396. This target is a minor-merger system and one galaxy in the system (SAMI609396B) is experiencing a burst of star formation. SAMI609396B is analogous to a high-redshift galaxy given its low-mass and high SFR. We detect prominent, spatially resolvable emission of three auroral lines: [S II] $\lambda \lambda 4069, 76$, [O III] $\lambda 4363$, and [S III] $\lambda 6312$ in SAMI609396B.

In this contribution, we focus on this notable case to study direct method metallicity and electron temperature in a spatially resolved manner. The presence of auroral lines from multiple ionic species allows us to investigate the common assumption of using an assumed temperature relation (e.g. $T_e(\text{[O II]}) - T_e(\text{[O III]})$ relation) on the spatial distribution of metallicity in galaxies. Additionally, comparisons to strong-line metallicity trends provide further insight into possible systematic effects in samples of gradients measured in the local and high-redshift Universe. Given the rarity of spatially resolved T_e studies at low redshift, and the relevance of this object to high-redshift comparisons, it warrants a detailed study of its own.

This work is organized as follows. In Section 2 we briefly describe the SAMI DR2 public release data, general properties of the SAMI609396 system, and selection of SAMI609396B. Our methodology for deriving spatially resolved electron temperature measurements is outlined in Section 3. In Section 4 we derive metallicity maps from three different ‘direct method’ approaches and four different strong-line methods and discuss the differences in spatial trends favoured by each. We discuss further caveats in Section 5 before summarizing and presenting conclusions in Section 6. Detailed descriptions of the derivation of global properties, spectral fitting, and emission line measurements are deferred to the Appendix. We also include a list of SAMI galaxies with visually identifiable auroral line emission in the Appendix. Throughout this paper we adopt the Planck Collaboration XIII (2016) cosmology: $\Omega_\Lambda = 0.692$, $\Omega_M = 0.308$, $\sigma_8 = 0.815$, and $H_0 = 67.8 \text{ km s}^{-1} \text{ Mpc}^{-1}$. All magnitudes are quoted in the *AB* magnitude system (Oke & Gunn 1983).

2 THE SAMI GALAXY SURVEY

We conducted a search for auroral lines in SAMI Galaxy Survey Public Data Release 2² (Bryant et al. 2015; Green et al. 2018; Scott et al. 2018). The SAMI Galaxy Survey (Bryant et al. 2015) is a large IFU survey targeting low-redshift ($z \lesssim 0.1$) galaxies with the Sydney – Australian Astronomical Observatory Multi-Object Integral Field

¹The Cl^{2+} and Ar^{3+} ions can provide similar temperature probes to complement O^{2+} measurements, however are usually too faint to be detectable.

²<https://sami-survey.org/abdr>

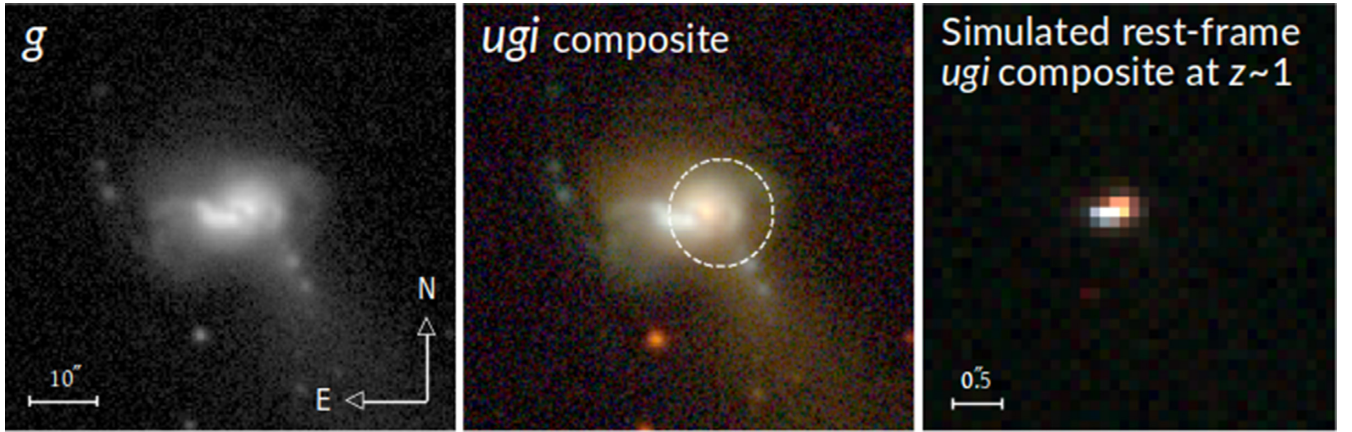


Figure 1. Left-hand panel: *g*-band imaging of the SAMI609396 merger system from SDSS. Middle panel: *ugi* RGB composite of the system. Prominent auroral line emission is associated with SAMI609396B, the lower-left object exhibiting strong blue colour in the *ugi* composite. The white dashed circle in the middle panel shows the field of view observed by the SAMI IFU. The 10'' scale given for the *g*-band image applies also for the middle panel and corresponds to approximately 3.8 kpc in physical distance. Right-hand panel: simulated rest-frame *ugi* colour composite after artificially redshifting the *u*-, *g*-, and *i*-band imaging to $z \sim 1$. After redshifting, these bandpasses correspond approximately to *HST* filters ACS/F606W, ACS/814W, and WFC3/F160W. The pixel scale in the simulated image is 0''.1, similar to that of *HST*/WFC3. The simulated depth of the image is similar to observations in 3D-*HST* (Yuan et al. 2020).

Spectrograph (Croom et al. 2012). Reduced SAMI data cubes are formed by sampling dithered hexabundle observations on to a regular grid (refer to Allen et al. 2015 and Sharp et al. 2015 for details). The SAMI aperture has a radius of approximately ~ 7.5 arcsec with a sampling of $0''.5 \times 0''.5$ spaxels. The true spatial resolution is limited by the seeing, recorded as $\text{FWHM}_{\text{PSF}} = 2.07$ arcsec (~ 790 pc) for SAMI609396. SAMI observes in two spectral bands. The blue arm covers the observed wavelength range from 3750 to 5750 Å at low spectral resolution ($R \sim 1808$, $\sigma v \sim 74$ km s $^{-1}$, at 4800 Å), while the red arm covers from 6300–7400 Å at medium resolution ($R \sim 4304$, $\sigma v \sim 29$ km s $^{-1}$, at 6850 Å) (e.g. Zhou et al. 2017). For more detailed information on the SAMI survey and data products, the reader is referred to the above references.

Among nine SAMI galaxies in which we visually identified the presence of up to three auroral lines ([S II] $\lambda\lambda 4069, 76$, [O III] $\lambda 4363$, and [S III] $\lambda 6312$), we highlight one notable case, SAMI609396 – a minor-merger system (Fig. 1). The remainder of this paper is focused on this object. The list of SAMI galaxies we compiled with identifiable auroral line emission can be found in Appendix A.

2.1 SAMI609396

SAMI609396 (SDSS J114212.25+002004.0) is identified as a minor merger in the Sloan Digital Sky Survey (SDSS) images (Fig. 1). The two merging galaxies are not deblended in the SDSS catalogue with the merger system having a total *r*-band magnitude of 13.95. The SAMI input catalogue gives the heliocentric redshift as $z = 0.01824$.

The merger signatures are evident from the colour difference and tidal tails. A visual inspection of the system shows one smaller galaxy exhibiting a strong blue colour, with a larger companion that is significantly redder (see Fig. 1, middle panel). Spatially resolved 1D spectra from the publicly available SAMI data cube show that the smaller galaxy in this system (SAMI609396B) is experiencing a burst of star formation associated with strong [O III] $\lambda 5007$ emission lines (Equivalent Width (EW) ~ 200 Å). Several prominent auroral emission lines ([S II] $\lambda\lambda 4069, 76$, [O III] $\lambda 4363$, and [S III] $\lambda 6312$) are detected in SAMI609396B. Using spatially resolved star formation rate (SFR) maps and photometry from SAMI (Appendix B), we derive SFR and M_* estimates for SAMI609396B of $4.21 \pm 0.30 M_\odot \text{ yr}^{-1}$

and $\log(M_*/M_\odot) = 9.18 \pm 0.05$. These values of SFR and M_* place SAMI609396B 1.3 dex above the local star formation ‘main-sequence’ (Renzini & Peng 2015).

2.1.1 SAMI609396B properties in the context of high-redshift galaxies

A number of galaxy properties have been shown to evolve systematically with redshift including SFR (e.g. Speagle et al. 2014), metallicity (e.g. Zahid et al. 2013; Sanders et al. 2020), ionization parameter (Sanders et al. 2016), and nebular emission line ratios (e.g. Kewley et al. 2013; Steidel et al. 2014). Given that placing observational constraints on high-redshift galaxies is comparably much more challenging than for local galaxies, there has been interest in obtaining observational constraints for ‘high-redshift analogues’ (e.g. Heckman et al. 2005; Cardamone et al. 2009; Green et al. 2014; Bian et al. 2016). These are galaxies at low-redshift with properties that emulate those observed in high-redshift galaxies. Given the rarity of auroral emission lines in IFU data, we consider that SAMI609396B is worthy of a detailed study on its own. However, we also consider how its properties compare to those seen in high-redshift galaxies.

As outlined above in Section 2.1, the SFR and M_* measurements for SAMI609396B are more than 1 dex above the local star-forming main sequence, more in line with values typical of galaxies at $z \gtrsim 1$. Global metallicity correlates positively with stellar mass at $z \sim 0$ (mass–metallicity relation; refer to Maiolino & Mannucci 2019 and references therein), and at fixed stellar mass, metallicity is seen to decrease with increasing redshift (Zahid et al. 2013; Sanders et al. 2020). According to a recent multidagnostic determination by Sanders et al. (2020), galaxies of a mass comparable to SAMI609396B ($\log(M_*/M_\odot) \approx 9.18$) would have a median metallicity of $12 + \log(\text{O}/\text{H}) = 8.55$ at $z \sim 0$, $12 + \log(\text{O}/\text{H}) = 8.26$ at $z \sim 2.3$, and $12 + \log(\text{O}/\text{H}) = 8.17$ at $z \sim 3.3$. Absolute metallicity values for individual galaxies are notoriously difficult to determine and depend strongly on the calibration used (e.g. Kewley & Ellison 2008). Although we do not take the step of applying the same metallicity calibration used by Sanders et al. (2020), according to the metallicities we derive for SAMI609396B in Section 4 we expect that

the metallicity of SAMI609396B would likely fall somewhere between the median values expected from the $z \sim 0$ and $z \sim 2.3$ samples.

Ionization parameters and electron densities in $z \sim 2.3$ galaxies have been shown to be systematically offset from local galaxies at fixed stellar mass (Sanders et al. 2016). Electron density is most commonly probed with the $[\text{S II}] \lambda 6716/\lambda 6731$ doublet ratio. MOSDEF galaxies at $z \sim 2.3$ were found by Sanders et al. (2016) to have a median $[\text{S II}]$ doublet ratio of 1.13, corresponding densities of around 290 cm^{-3} in the S^+ zone of emitting nebulae, much higher than typical SDSS values ($[\text{S II}] \lambda 6716/\lambda 6731 = 1.41$; density of 26 cm^{-3}). We measure a global $[\text{S II}]$ ratio of 1.29 for SAMI609396B, corresponding to a density of 118 cm^{-3} , placing SAMI609396B between the low- and high-redshift sample medians. Given the scatter about those median values in both the MOSDEF and SDSS samples (figs 4 and 5 in Sanders et al. 2016), it is difficult to draw conclusions about how SAMI609396B compares to the two populations based on density. Using the O_{32} strong-line ratio as a tracer for ionization parameter, Sanders et al. (2016) found that, like SDSS galaxies, $z \sim 2.3$ MOSDEF galaxies show a trend of decreasing ionization parameter with increasing stellar mass. They find the slope of this relation to be very similar to that of SDSS galaxies, however with a ~ 0.6 dex offset towards higher O_{32} at fixed stellar mass in the $z \sim 2.3$ sample (fig. 8 in Sanders et al. 2016). Given the stellar mass derived for SAMI609396B ($\log(M_*/M_\odot) \approx 9.18$), SDSS galaxies have a median value of $\text{O}_{32} = -0.25$, while MOSDEF galaxies with comparable mass have much higher values ($\text{O}_{32} = 0.28$). We measure $\text{O}_{32} = 0.14$ for SAMI609396B, 0.39 dex higher than the median SDSS value and 0.14 dex below the median of $z \sim 2.3$ MOSDEF galaxies.

Recent studies have found an offset in the locus inhabited by high-redshift galaxies on the N2-BPT diagram (Baldwin, Phillips & Terlevich 1981) with high-redshift galaxies exhibiting higher $[\text{O III}]/\text{H}\beta$ at fixed $[\text{N II}]/\text{H}\alpha$ (Kewley et al. 2013; Steidel et al. 2014). We find that BPT line ratios observed for SAMI609396B to be within the range of local galaxies. Our analysis of the spatially resolved BPT diagram of SAMI609396B is discussed in detail in Section 5.

To summarize, we find that the physical properties (SFR and ISM conditions) of SAMI609396B tend to be offset from median $z \sim 0$ values, although are generally less extreme than $z \sim 2$ galaxies. In combination with the high $\text{EW}([\text{O III}])$, we consider that the physical properties of SAMI609396B might be analogous to intermediate-redshift ($0 < z \lesssim 1$) galaxies. Low-mass galaxies like SAMI609396B are extremely difficult to resolve at high redshift. To visually demonstrate what a system like SAMI609396 would look like at a higher redshift, we simulate the angular size and morphology of SAMI609396 at $z \sim 1$ using similar techniques to those detailed in Yuan et al. (2020). The redshifted morphology is presented on the right-hand panel of Fig. 1. In order to resolve a low-mass system like SAMI609396B at $z \sim 1$ with comparable physical resolution of SAMI, a minimal angular resolution of 0.1 arcsec is required. Such a fine resolution can be achieved either through ground-based adaptive optics or space instruments. The faintness of these low-mass systems also means the need for next-generation facilities such as *JWST*/NIRSpec and ground-based ELTs.

2.2 SAMI DR2: Value-added data products

SAMI DR2 includes a number of publicly available value-added data products, which we use to guide our initial understanding of the SAMI609396 system. Fig. 2 shows publicly available maps for the

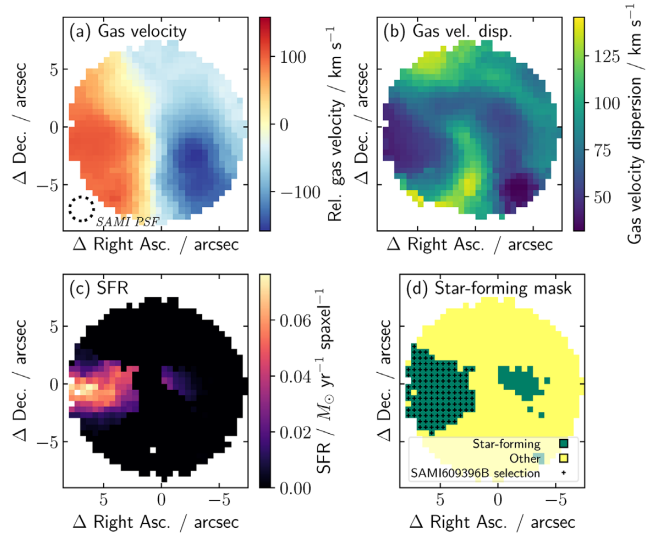


Figure 2. Publicly available value-added data products from SAMI DR2. (a) Gas velocity from 1-component fitting. (b) Gas velocity dispersion from 1-component fitting. (c) Per spaxel star-formation rate (Medling et al. 2018). (d) Star-forming mask. The large star-forming dominated region denoted with black ‘+’ symbols in (d) is characterized by very high SFR, velocity dispersions of $\sim 30\text{--}80 \text{ km s}^{-1}$, and relative velocities of $\sim 100 \text{ km s}^{-1}$ (in the scale of panel a). This region, designated SAMI609396B, is spatially associated with observed auroral lines and is the target of our investigation. The black dotted circle in panel (a) indicates the point-spread function measured for this SAMI observation and applies to all panels.

gas velocity, gas velocity dispersion, and star-formation rate (Panels a–c) derived from 1-component fits.

Panel (d) of Fig. 2 shows a star-formation mask, determined according to Kewley et al. (2006) based on BPT & VO87 diagnostic diagrams (Baldwin et al. 1981; Veilleux & Osterbrock 1987), with green denoting spaxels passing selection as ‘star-formation dominated’. Fig. 2 shows that much of the SAMI field of view is dominated by emission from non-star-forming sources (yellow spaxels; ‘other’). The yellow spaxels have higher velocity dispersion compared with star-forming dominated regions, characteristic of emission from shock-heated gas. The BPT diagram and the origin of emissions in these regions are discussed further in Section 5.2.

The prominent auroral line emission we identify is spatially associated with the large star-formation dominated region in the left-hand (eastern) portion of the star-formation mask. This region has a median rest-frame gas velocity of $v_{\text{gas}} \approx 100 \text{ km s}^{-1}$ (refer to scale in Fig. 2), a velocity dispersion of range $\sigma_{\text{gas}} \approx 30\text{--}80 \text{ km s}^{-1}$, and high a star-formation rate (median SFR surface density $\approx 0.97 \text{ M}_\odot \text{ yr}^{-1} \text{ kpc}^{-2}$).

We designate this object as ‘SAMI609396B’ and define its selection within the SAMI609396 datacube as including spaxels labelled as star-formation dominated with $v_{\text{gas}} > 0$, denoted by black ‘+’ symbols in panel (d) of Fig. 2. Global SFR and stellar mass estimates for SAMI609396B and its companion galaxy are provided in Table 1. Details of how these are derived are provided in Appendix B.

3 SPATIALLY RESOLVED ELECTRON TEMPERATURE

The electron temperature (T_e) and electron density (n_e) are fundamental physical parameters in understanding the emission line

³ $\text{O}_{32} = [\text{O III}] \lambda\lambda 4959, 5007 / [\text{O III}] \lambda\lambda 3726, 29$ in this context

Table 1. Global properties of SAMI609396B and its companion.

Right ascension	11 ^h 42 ^m 12 ^s .25
Declination	+00°20′ 04″.04
z	0.01824
SAMI609396B:	
SFR ($M_{\odot} \text{ yr}^{-1}$) ^a	4.21 ± 0.30
$\log(M_*/M_{\odot})$	9.18 ± 0.05
Companion:	
SFR ($M_{\odot} \text{ yr}^{-1}$) ^a	0.32 ± 0.08
$\log(M_*/M_{\odot})$	9.88 ± 0.07

Notes.^aSFR measurement for area within SAMI FoV (see Fig. 1).

This is best considered as a lower bound.

physics of ionized nebulae. Abundance measurements from collisionally excited lines in H II regions are very sensitive to these parameters. For this reason, chemical abundances derived following explicit measurements of T_e and n_e are generally used as a baseline calibration for understanding the chemistry of ionized nebulae (e.g. Maiolino & Mannucci 2019).

This is generally achieved with the so-called ‘direct method’ via measurement of an auroral emission line and a strong nebular line of the same ionic species. This is most commonly applied to the O^{2+} ion using the [O III] $\lambda 4363/\lambda 5007$ ratio, which is primarily sensitive to T_e (its n_e dependence is minimal over the density range of typical H II regions). Within the typical rest-frame near-ultraviolet to near-infrared wavelength range observed for galaxies, auroral line ratios may be observable for a number of ionic species including O^+ , N^+ , S^{2+} , and S^+ , each of which probe different zones within the emitting H II regions according to the distribution of those ions within the nebular structure. Although we detect auroral lines from three ionic species in SAMI609396B ([S II], [O III], and [S III]), we are able to derive electron temperature for only the [O III] and [S II] ionization zones as we lack the spectral coverage to measure the [S III] $\lambda 9069$ and [S III] $\lambda 9531$ strong lines required to derive T_e ([S III]).

3.1 Auroral emission line measurements

We derive flux maps for auroral lines from three ionic species ([S II] $\lambda\lambda 4069, 76$, [O III] $\lambda 4363$, and [S III] $\lambda 6312$) identified in the SAMI609396 data cube, as the SAMI DR2 value-added data products do not include emission line maps for these fainter lines. We concomitantly re-derive strong emission line fluxes, rather than use SAMI DR2 emission line maps, ensuring self-consistency in our line ratio measurements. These flux maps are generated by applying standard methods to each spaxel, first fitting the stellar continuum, and then simultaneously fitting profiles to each emission line included in our analysis. Details of this spectral fitting are provided in Appendix C.

We obtain $S/N \sim 3\text{--}15$ in individual spaxels for each of [O III] $\lambda 4363$, [S II] $\lambda\lambda 4069, 76$, and [S III] $\lambda 6312$ across the majority of the spatial region selected as SAMI609396B. We identify from visual inspection some degree of blending between [O III] $\lambda 4363$ and a neighbouring faint [Fe II] emission line at $\lambda 4360$, similar to that observed in other recent studies (e.g. Curti et al. 2017; Arellano-Córdova & Rodríguez 2020; Berg et al. 2020). We find that the [O III] $\lambda 4363$ line is brighter than the $\lambda 4360$ feature by a factor of ~ 2 and that with the spectral resolution of the blue arm of the SAMI spectrograph we are able to reliably recover the [O III] $\lambda 4363$ flux. Our efforts to test the reliability of our [O III] $\lambda 4363$ flux measurements are outlined in detail in Appendix C3.

3.2 [O III] electron temperature

The emission line ratio most widely used to determine the electron temperature with the direct method is the [O III] $\lambda 4363$ / [O III] $\lambda 5007$ ratio. Despite the primary dependence of this [O III] ratio on temperature, the residual density dependence is often accounted for by measurement of a density sensitive line ratio, typically [S II] $\lambda 6716$ / [S II] $\lambda 6731$. Izotov et al. (2006) use relations derived for these aforementioned [O III] and [S II] line ratios (equations 1 and 2 in that reference) in an iterative manner, solving simultaneously for T_e and n_e . This iterative approach is shared by the `getCrossTemDen` routine in the `PyNEB` package (Luridiana, Morisset & Shaw 2015), which allows for a flexible array of temperature- and density-sensitive line ratios.

However, it is important to consider that neither temperature nor density is expected to be constant throughout H II regions. Additionally, emission from different ionic species may not be co-spatial. Certainly, [S II] emission is expected to arise from the outer regions of nebulae, thus densities measured from the [S II] line ratio do not necessarily provide a good indication of the density of the [O III] emission region (see fig. 2 in Kewley et al. 2019).

Given these uncertainties, Nicholls et al. (2020) instead propose a simplified approach in which T_e is derived from an empirical relation of the auroral line ratio, derived from H II region modelling, forgoing any attempt to account for n_e , suggesting that any improvements in temperature insight are outweighed by uncertainties induced by density variations and lack of co-spatiality.

Given the ~ 1 kpc spatial resolution of SAMI, we are unable to resolve individual H II regions, adding to the uncertainties described above. Thus, we use this simplified approach to derive our T_e from the [O III] $\lambda 4363$ / [O III] $\lambda 5007$ ratio according to the relation given in Nicholls et al. (2020). This relation is shown as equation (1) here:

$$\log_{10}(T_e([\text{O III}])) = \frac{3.3027 + 9.1917x}{1.0 + 2.092x - 0.1503x^2 - 0.0093x^3}, \quad (1)$$

where $x = \log_{10}(f_{4363}/f_{5007})$, with f_x referring to a line flux measurement of a collisionally excited line with rest-frame wavelength X Å, and T_e is in units of K. The derived [O III] temperature map for spaxels with [O III] $\lambda 4363$ of $S/N > 3$ is shown in Fig. 3.

3.3 [S II] electron temperature

In addition to T_e ([O III]), spatially resolved measurements of the [S II] auroral lines allow us to measure T_e ([S II]) from the [S II] $\lambda\lambda 4069, 76$ / [S II] $\lambda\lambda 6716, 31$ ratio.

Modelling indicates that at the low density limit ($1 < n_e < 50 \text{ cm}^{-3}$), the residual density dependence of the [S II] $\lambda\lambda 4069, 76$ / [S II] $\lambda\lambda 6716, 31$ ratio is minimal. In contrast to the [O III] case, this [S II] temperature diagnostic is co-spatial with the [S II] density diagnostic, meaning that we are able to make a more reliable estimate of the density. The n_e values for SAMI609396 obtained with the [S II] $\lambda 6716$ / [S II] $\lambda 6731$ ratio (equation 3 in Proxauf, Öttl & Kimeswenger 2014) are shown in Fig. 4 (b). We find the median electron density to be $\tilde{n}_e = 92 \text{ cm}^{-3}$. This value is above the [S II] low density limit, indicating that [S II] $\lambda\lambda 4069, 76$ / [S II] $\lambda\lambda 6716, 31$ will have a residual density dependence. None the less, we derive the [S II] temperature with a similar approach to that outlined in Section 3.2 with a new rational polynomial fit to modelling data assuming a density of $n_e = 100 \text{ cm}^{-3}$. This fit is given in equation (2) where $x = \log_{10}[(f_{4069} + f_{4076})/(f_{6716} + f_{6731})]$ and T_e is in units of K.

$$\log_{10}(T_e([\text{S II}])) = \frac{-0.08891 + 2.06354x + 3.38680x^2 + 0.10754x^3}{0.1 + 0.78000x + 0.94404x^2}. \quad (2)$$

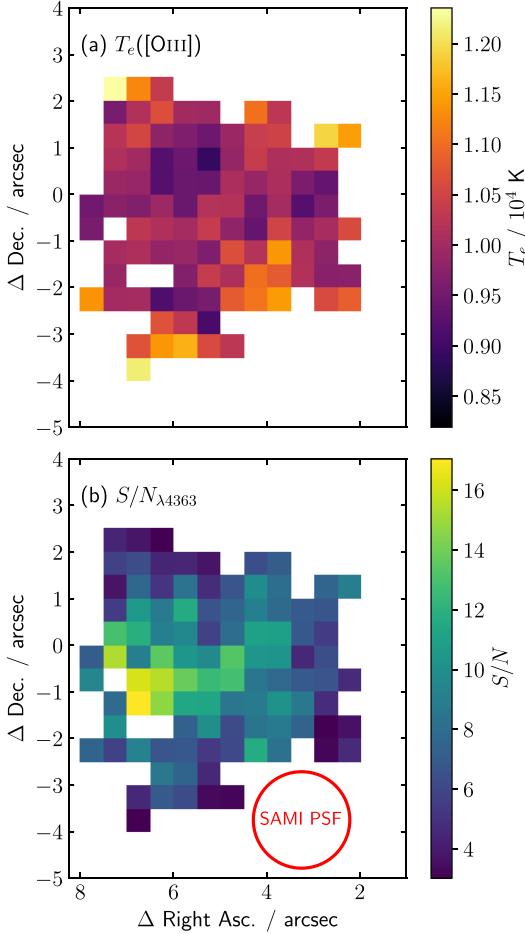


Figure 3. Top: Electron temperature map derived from the $[\text{O III}]\lambda 4363 / [\text{O III}]\lambda 5007$ ratio (see Section 3.2). Bottom: Measured signal-to-noise of $[\text{O III}]\lambda 4363$ auroral line. The red circle depicts the FWHM PSF of this SAMI data cube and applies to both panels. The large scale spatial variations in T_e do not appear to correlate with $[\text{O III}]\lambda 4363$ S/N .

$T_e([\text{S II}])$ values obtained for SAMI609396 are compared with $T_e([\text{O III}])$ values in Fig. 4. Panels (a) and (b) show maps of $T_e([\text{S II}])$ and $T_e([\text{O III}])$, respectively, for spaxels where the relevant auroral line is detected with $S/N > 5$. Panel (c) shows the direct comparison of $T_e([\text{S II}])$ and $T_e([\text{O III}])$ values on a spaxel-by-spaxel basis. We observe that a majority of points in panel (c) of Fig. 4 lie below the line of $T_e([\text{S II}]) = T_e([\text{O III}])$ (i.e. higher $T_e([\text{O III}])$ than $T_e([\text{S II}])$). The large blue and red points in Fig. 4(c) show derived $T_e([\text{S II}])$ and $T_e([\text{O III}])$ electron temperatures for two mock apertures which correspond to the regions shown as blue and red dashed circles in Panel (a). These aperture temperatures appear to indicate that $T_e([\text{S II}])$ and $T_e([\text{O III}])$ do not exhibit strong positive correlation across different spatial regions of SAMI609396B. The implications of this temperature relation for metallicity measurement are discussed further in Section 4.

4 SPATIAL TRENDS IN METALLICITY

In Section 3, we derived spatially resolved electron temperature (T_e) measurements. Here we use these T_e measurements to determine direct method oxygen abundances under three different sets of assumptions, showing that derived spatial variations in metallicity can be very sensitive to the assumed internal H II region tempera-

ture structure. Additionally we derive spatially resolved strong-line metallicities and discuss differences in observed spatial trends.

4.1 Direct method metallicity

Since the abundance of neutral oxygen (O^0) and oxygen in ionization states higher than O^{2+} is expected to be negligible in H II regions, we assume that the total oxygen abundance can be approximated as equation (3):

$$\frac{\text{O}}{\text{H}} = \frac{\text{O}^+}{\text{H}^+} + \frac{\text{O}^{2+}}{\text{H}^+}. \quad (3)$$

We derive abundances of these two ionization states of oxygen using the following analytic relations set out in Pérez-Montero (2017):

$$12 + \log \left(\frac{\text{O}^{2+}}{\text{H}^+} \right) = \log \left(\frac{f_{4959} + f_{5007}}{f_{\text{H}\beta}} \right) + 6.1868 + \frac{1.2491}{t(\text{O}^{2+})} - 0.5816 \cdot \log(t(\text{O}^{2+})). \quad (4)$$

$$12 + \log \left(\frac{\text{O}^+}{\text{H}^+} \right) = \log \left(\frac{f_{3726} + f_{3729}}{f_{\text{H}\beta}} \right) + 5.887 + \frac{1.641}{t(\text{O}^+)} - 0.543 \cdot \log(t(\text{O}^+)) + 0.000114 \cdot n_e, \quad (5)$$

where $t(\text{O}^{2+}) = T_e([\text{O III}])/10^4$ K, $t(\text{O}^+) = T_e([\text{O II}])/10^4$ K, n_e is the electron density measured by the $[\text{S II}]\lambda 6716 / \lambda 6731$ ratio, and f_X refers to a line flux measurement of the $\text{H}\beta$ Balmer line or a collisionally excited line with rest-frame wavelength X Å. Deriving O^{2+}/H^+ in this way requires only $[\text{O III}]\lambda\lambda 4959, 5007$ and $\text{H}\beta$ emission line fluxes in addition to the $T_e([\text{O III}])$ values derived in Section 3.2. On the other hand, the O^+/H^+ abundance from equation (5) calls for $T_e([\text{O II}])$, which we do not directly measure. Additionally, O^+/H^+ has residual dependence on n_e , although we simply adopt the same fixed density $n_e = 100 \text{ cm}^{-3}$ used in the temperature calculations in Section 3.2. Note that our derived metallicity values vary by less than 0.01 dex with changes in adopted density, provided those are below $n_e < 200 \text{ cm}^{-3}$.

Unlike $T_e([\text{O III}])$, we do not directly measure $T_e([\text{O II}])$, since we are unable to detect either the $[\text{O II}]\lambda\lambda 7319, 30$ or $[\text{O II}]\lambda\lambda 2470 + \text{doublets}$. A favourable alternative is to use temperatures derived from other ionic species, especially $[\text{N II}]$ or $[\text{S III}]$, to probe the temperature structure (e.g. Berg et al. 2020). However, given the faintness of auroral lines it is common that an observation may enable measurement of only the $[\text{O III}]$ temperature zone. In this scenario, a $T_e([\text{O II}])$ estimate can be obtained by adopting an empirical $T_e([\text{O II}]) - T_e([\text{O III}])$ relation, for which a number of calibrations exist (e.g. Izotov et al. 2006; López-Sánchez et al. 2012). Despite expanding the number of observations for which direct metallicities can be derived, Yates et al. (2020) (Y20 hereafter) find that using $T_e([\text{O II}]) - T_e([\text{O III}])$ relations can underestimate the direct metallicity by more than 0.5 dex for low-ionization systems, highlighting the importance of constraining the internal temperature structure of H II regions where possible. Additionally, Y20 provide an empirical correction for this effect based on the $[\text{O III}]/[\text{O II}]$ strong line ratio.

For this analysis, we determine our total oxygen abundance maps in three ways. Each differs in its approach to handling the O^+/H^+ abundance, while in all three cases the O^{2+}/H^+ abundance is determined from equation (4) and our direct measurement of $T_e([\text{O III}])$. For the remainder of this paper, metallicities derived in these three ways will be abbreviated as $Z_{\text{Te;LS12}}$, $Z_{\text{Te;Y20}}$ and $Z_{\text{Te;SH}}$ (where $Z = 12 + \log(\text{O}/\text{H})$), described as follows:

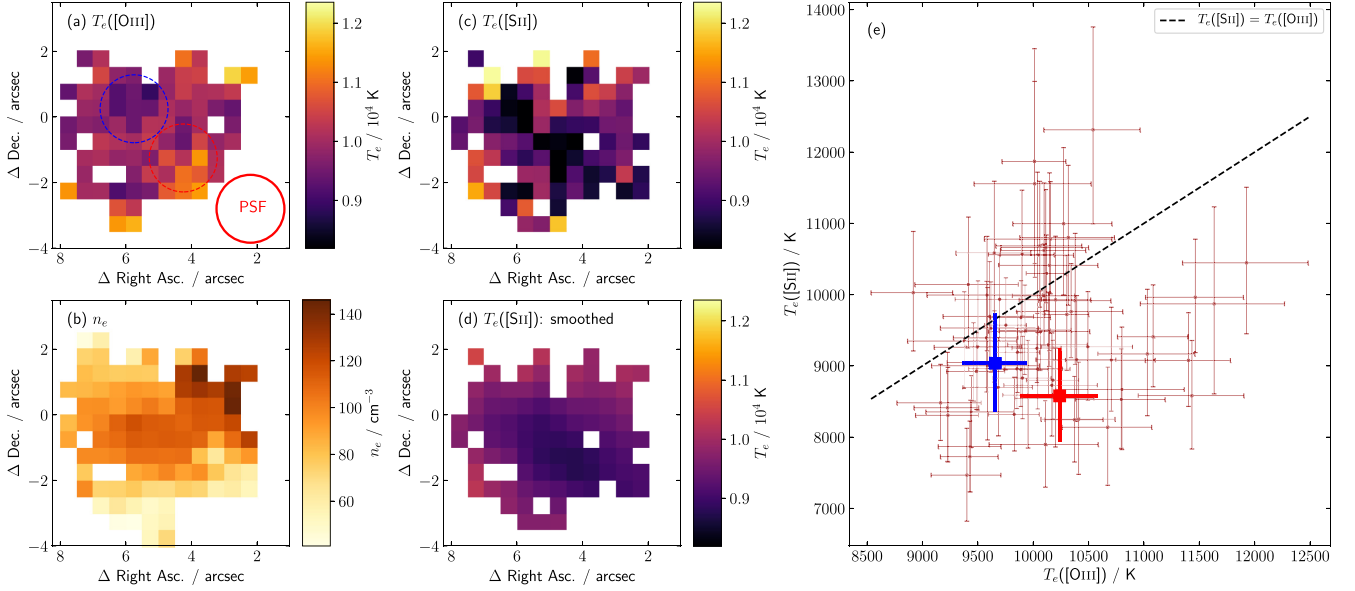


Figure 4. Comparison of $T_e([\text{O III}])$ and $T_e([\text{S II}])$ electron temperature values. (a) map of $T_e([\text{O III}])$ values for spaxels with $S/N > 5$ for $[\text{O III}] \lambda 4363$. The red circle labelled ‘PSF’ has diameter equal to the FWHM of the SAMI PSF for this observation and applies to panels (a–d). (b) electron density derived from the $[\text{S II}] \lambda 6716 / \lambda 6731$ ratio. (c) map of $T_e([\text{S II}])$ values for spaxels with $S/N > 5$ for $[\text{S II}] \lambda \lambda 4069, 76$. (d) map of $T_e([\text{S II}])$ from panel (c) smoothed with a Gaussian filter. (e): The brown points show values of $T_e([\text{S II}])$ and $T_e([\text{O III}])$ for individual spaxels with $S/N > 5$ on both auroral lines. Error bars shown reflect only measurement uncertainty and do not include associated modelling uncertainties. Temperatures derived for two mock apertures (indicated by blue and red dashed circles in panel a) are shown as the blue and red points in panel (e).

(i) $Z_{\text{Te;LS12}}: \text{O}^+/\text{H}^+$ is determined using $T_e([\text{O II}])$ derived from $T_e([\text{O III}])$ using the relation outlined in López-Sánchez et al. (2012) (equation 6).⁴ This is the most commonly adopted method.

(ii) $Z_{\text{Te;Y20}}: \text{As for } Z_{\text{Te;LS12}}, \text{ with the subsequent application of the Y20 empirical correction, based on } [\text{O III}]/[\text{O II}] \text{ strong-line ratio (equation 7). This is a relatively new correction and has not been widely implemented in literature yet.}$

(iii) $Z_{\text{Te;SII}}: \text{O}^+/\text{H}^+$ is determined with $T_e([\text{O II}])$ derived instead from $T_e([\text{S II}])$ using the assumption $T_e([\text{O II}]) = T_e([\text{S II}])$. This is uniquely enabled by the detection of $[\text{S II}]$ auroral lines in this study.

4.1.1 Empirical $T_e([\text{O II}]) - T_e([\text{O III}])$ relation

For $Z_{\text{Te;LS12}}$ we adopt the $T_e([\text{O II}]) - T_e([\text{O III}])$ relation as calibrated by López-Sánchez et al. (2012), given in equation (6):

$$T_e[\text{O II}] = T_e[\text{O III}] + 450 - 70 \cdot \exp[(T_e[\text{O III}]/5000)^{1.22}] \quad (6)$$

Deriving $T_e([\text{O II}])$ in this way and applying equations (4) and (5) we obtain the total oxygen abundance map shown in panel (a) of Fig. 5. The spatial structure of this map reflects that of the temperature map derived in Fig. 3 and favours a strong trend in metallicity across the region of the highest signal to noise (Fig. 5d).

The measurement uncertainty is dominated by the flux uncertainty of the $[\text{O III}] \lambda 4363$ emission line to the point where the measurement uncertainty contribution from the high S/N $[\text{O III}]$, $[\text{O II}]$, and $\text{H}\beta$ strong lines can be ignored. We see no obvious correlation between the S/N of $[\text{O III}] \lambda 4363$ and $T_e([\text{O III}])$ (Fig. 3). Increasing the minimum S/N cut on the $[\text{O III}] \lambda 4363$ auroral line from $S/N > 3$ to $S/N > 8$ changes the median metallicity by less than 0.005 dex.

⁴We note that alternative $T_e([\text{O II}]) - T_e([\text{O III}])$ relations, including the equations from Izotov et al. (2006), do not significantly affect the metallicity morphology obtained for SAMI609396B.

Together, these give us confidence that observed spatial variations in metallicity are not artefacts from measurement noise, although the effects of modelling uncertainty are discussed over the coming sections.

4.1.2 Empirical O^+ abundance correction

Yates et al. (2020) provide an empirical correction based on the observed $[\text{O III}]/[\text{O II}]$ line ratio given by equation (7),

$$Z_{\text{Te;Y20}} = Z_{\text{Te;LS12}} - 0.71 \cdot (\text{O32} - 0.29), \quad (7)$$

where $Z_{\text{Te;Y20}}$ and $Z_{\text{Te;LS12}}$ are corrected and uncorrected values of $12 + \log(\text{O}/\text{H})$ respectively; $\text{O32} = \log([\text{O III}] \lambda \lambda 4959, 5007 / [\text{O II}] \lambda \lambda 3726, 9)$ and the correction is applied only when $\text{O32} \leq 0.29$.

Values of O32 across SAMI609396B fall in the range for which this correction will be non-zero. Our direct metallicity map after Y20 correction is shown in Fig. 5(b). Spatial variations in the O32 ratio result in a flattening of the spatial trend after application of this correction.

We note that, in addition to the empirical correction described here (‘Y20 correction’), Yates et al. (2020) also outlined a novel method for determining semidirect metallicities (‘Y20 method’) in which $T_e([\text{O II}])$ and metallicity are solved for simultaneously, rather than sequentially. This Y20 method then also requires subsequent application of the Y20 correction if $\text{O32} \leq 0.29$, as above. Note that fig. 6 in Yates et al. (2020) shows that the abundance deficit at low O^{++}/O^+ , which the Y20 correction adjusts for, is present to varying degrees for all $T_e([\text{O II}]) - T_e([\text{O III}])$ relations considered in that work.

We find the Y20 method gives a two-valued solution for SAMI609396B which may require an additional prior to select the best metallicity solution. We found that applying the Y20 method as

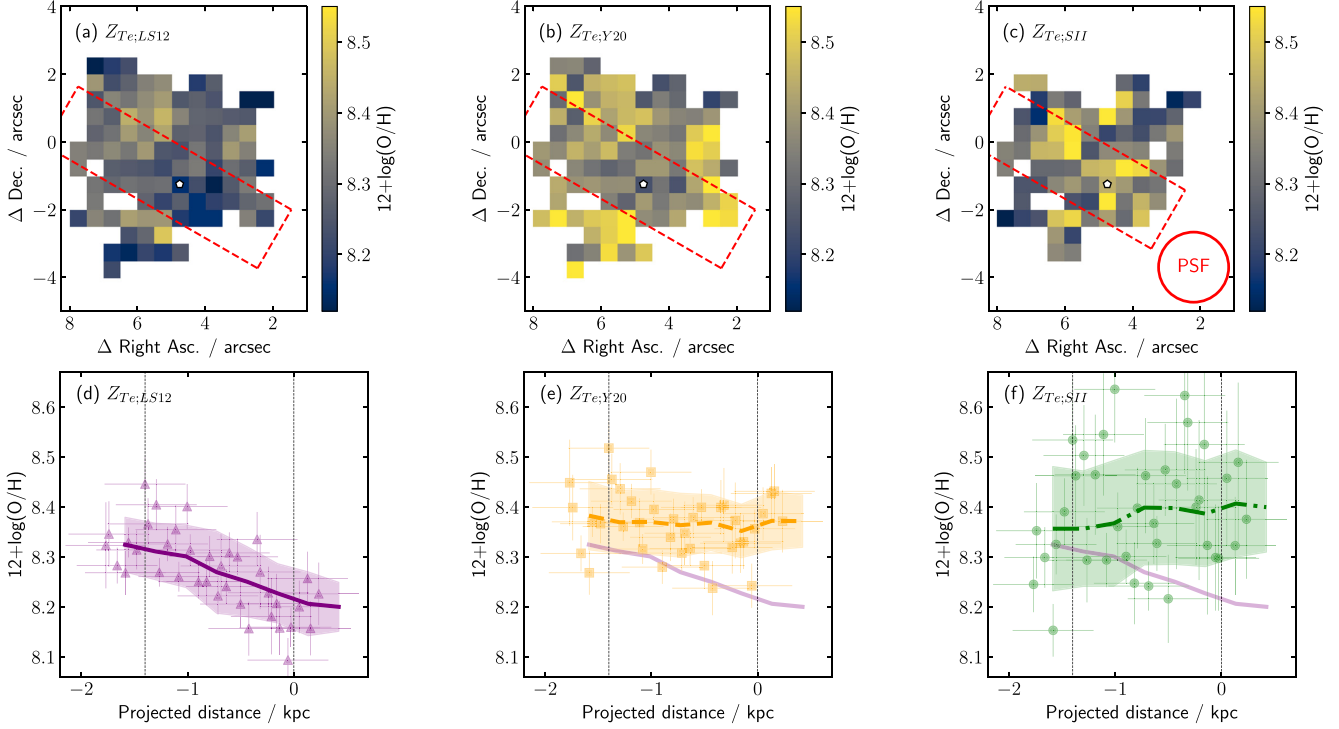


Figure 5. Observed spatial trends in direct method metallicity depend strongly on temperature structure assumptions. Direct method metallicity maps (panels a–c) and spatial metallicity trends (d–f) are shown for SAMI609396B under three different T_e ([O II]) temperature assumptions. Panels (a, d) show $Z_{Te,LS12}$: where T_e ([O II]) is derived from T_e ([O III]) via the relation of López-Sánchez et al. (2012) (equation 6). Panels (b, e) show $Z_{Te,Y20}$: derived as for $Z_{Te,LS12}$ with the additional step of applying the empirical correction of Y20 based on O32. Panels (c, f) show $Z_{Te,SII}$: metallicity is derived assuming T_e ([O II]) = T_e ([S II]). See Section 4.1 for details. Maps in panels (a–b) include spaxels with $S/N_{\lambda 4363} \geq 3$, while panel (c) additionally excludes spaxels with $S/N_{\lambda 4069} < 3$. The red circle in panel (c) shows the FWHM of the SAMI PSF and applies to panels (a–c). The dashed red rectangles in panels (a–c) span the region of highest S/N for the [O III] $\lambda 4363$ line and defines the spatial region examined in panels (d–f). Panels (d–f) show individual points for which $S/N_{\lambda 4363} > 5$. Trend lines indicate running medians of the points shown. Vertical error bars on individual points reflect only measurement uncertainties and are dominated by auroral line measurements.

originally outlined favoured the lower value of these two solutions which yielded a gradient comparable to that obtained from our $Z_{Te,Y20}$ approach here, albeit with a much lower normalization (~ 0.3 dex). We found that the normalization of the upper-branch solution was in better agreement with our other determinations outlined here, however the spatial trend arising from this upper-branch solution is more difficult to interpret. Discussion of our implementation of the Yates et al. (2020) method and its two-valued nature is deferred to Appendix D.

4.1.3 O^+ abundance with T_e ([S II])

The [S II] temperature samples a relatively narrow zone from the outer regions of nebulae and is consequently not widely used to constrain the temperature profile of emitting H II regions. However, Croxall et al. (2016) found general agreement of T_e ([S II]) with T_e ([O II]) and T_e ([N II]) in H II regions in NGC 5457. In the absence of the [S III] strong-lines, the [N II] auroral lines, or any other temperature probes, T_e ([S II]) affords our only direct probe of the internal temperature structure of H II regions in SAMI609396B.

We make the simplified assumption that T_e ([O II]) = T_e ([S II]) and update our total oxygen abundance using the measured T_e ([S II]) map (Fig. 4c) to re-derive our O^+/H^+ values. These updated oxygen abundances are shown in Fig. 5(c), spanning a slightly smaller spatial extent due to the additional requirement of [S II] auroral line signal to noise. The spatial trend shown in Fig. 5(f) is seen to be opposite

of that in Panel (d) where O^+/H^+ was derived using an empirical temperature relation, albeit with a larger scatter.

This stark reversal can be explained by the T_e ([S II]) – T_e ([O II]) trends observed in Fig. 4. Deriving T_e ([O II]) from a relation with T_e ([O III]) assumes that such a relation is fixed across the spatial region covered. This would mean that regions with elevated T_e ([O III]) would also show increased T_e ([O II]). However, the apertures plotted in panel (e) of Fig. 4 (blue and red bold points) show that despite the increase in T_e ([O III]) from the ‘blue’ aperture to the ‘red’ aperture, measured T_e ([S II]) instead decreases (albeit with large uncertainties). This suggests the absence of a strong positive correlation between these temperatures across the spatial region and highlights the limitations of applying empirical temperature relations to measure spatial metallicity trends. This is likely driven by variations in the ionization structure (i.e. O^{2+}/O^+ abundance ratio) and also explains the observed variations in O32 ratio that lead to the flattening of the spatial trend observed after applying the Y20 correction. We discuss this further in Section 4.3.

4.2 Strong-line metallicity

In Fig. 6 we compare four different strong-line metallicity maps with $Z_{Te,LS12}$ and $Z_{Te,Y20}$ direct method metallicity maps derived in Section 4.1. Strong-line metallicities are derived using a selection of widely strong-line diagnostics, defined in equations (8)–(13):

$$N2O2 = \log_{10} ([N II]/[O II]) \quad (8)$$

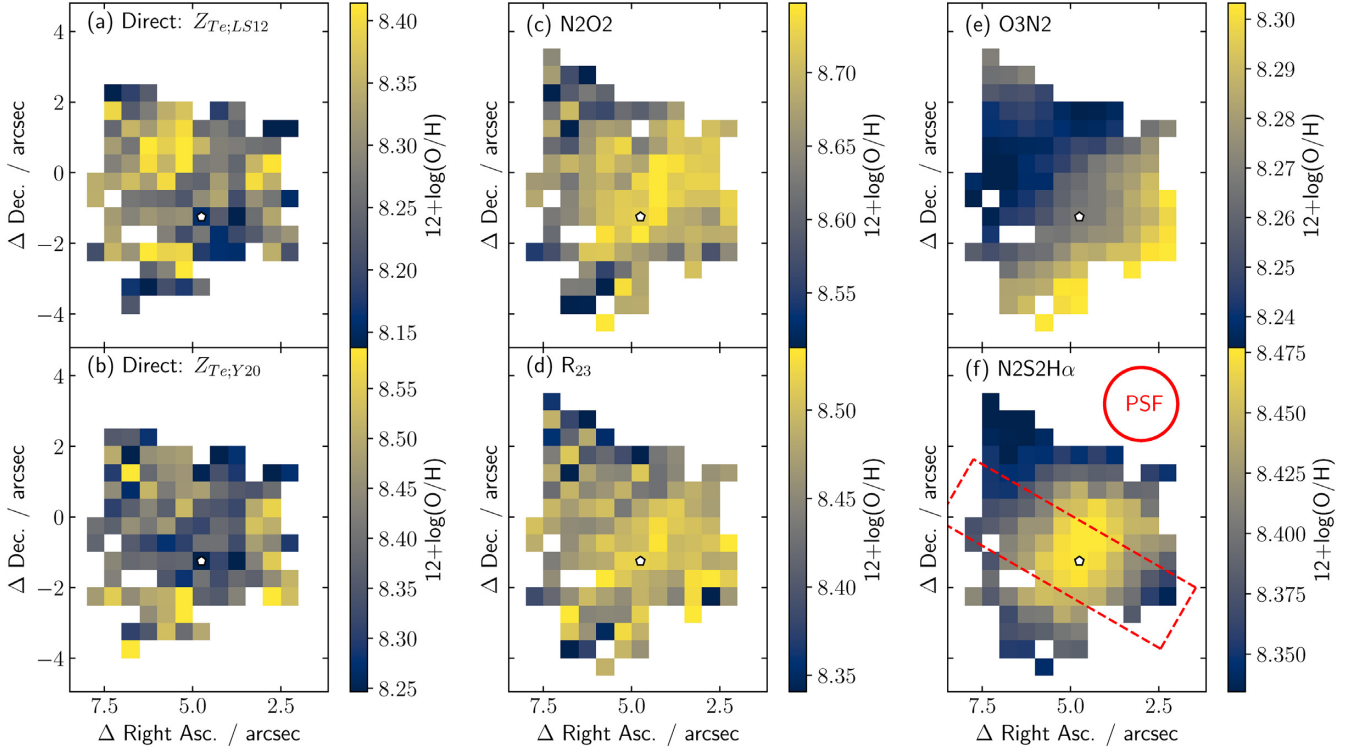


Figure 6. Direct method and strong-line oxygen abundance maps for the star-formation selected region corresponding to SAMI609396B. (a) Direct method metallicity using T_e values derived from $[\text{O III}] \lambda 4363 / \lambda 5007$ ratio (see Section 4.1). (b) Direct method metallicity after applying the empirical correction of Yates et al. (2020) (see Section 4.1.2). (c) iterative solution for metallicity, solved simultaneously for metallicity with N2O2 and ionization parameter with O32 using calibrations from Kewley et al. (2019). (d) metallicity from R_{23} strong-line diagnostic using calibration from Curti et al. (2020a). (e) metallicity derived from O3N2 using calibration from Marino et al. (2013). (f) metallicity derived from the N2S2H α diagnostic as outlined in Dopita et al. (2016). The peak i -band flux from SDSS imaging is marked in each panel with a white pentagon. FWHM of the spatial PSF is shown by the red circle in panel (f). The slit shown in panel (f) spans the region of highest S/N for the $[\text{O III}] \lambda 4363$ line and is examined in detail in Fig. 7.

$$\text{O32} = \log_{10}([\text{O III}]/[\text{O II}]) \quad (9)$$

$$R_{23} = \log_{10}\left(\frac{[\text{O III}] \lambda 4959 + [\text{O III}] \lambda 5007 + [\text{O II}]}{H\beta}\right) \quad (10)$$

$$\text{N2} = \log_{10}([\text{N II}]/H\alpha) \quad (11)$$

$$\text{O3N2} = \log_{10}([\text{O III}]/H\beta) - \text{N2} \quad (12)$$

$$\text{N2S2H}\alpha = \log_{10}([\text{N II}]/[\text{S II}]) - 0.264 \cdot \text{N2}, \quad (13)$$

where $[\text{N II}] = [\text{N II}] \lambda 6583$, $[\text{O II}] = ([\text{O II}] \lambda 3726 + [\text{O II}] \lambda 3729)$, $[\text{S II}] = ([\text{S II}] \lambda 6716 + [\text{S II}] \lambda 6731)$, and $[\text{O III}] = [\text{O III}] \lambda 5007$ unless otherwise specified. We use strong-line calibrations based on a mixture of theoretical and observational calibrations, outlined as follows:

(i) **N2O2:** We use the theoretical calibration provided in Kewley et al. (2019) to solve iteratively for metallicity and ionization parameter using the N2O2 (equation 8) and O32 (equation 9) diagnostic line ratios.

(ii) **R_{23} :** We use the calibration provided by Curti et al. (2020a) based on direct method measurements of stacked SDSS galaxies. The R_{23} ratio (equation 10) is two-valued with a turnover at around $12+\log(\text{O}/\text{H}) = 8.1$. Using N2 (equation 11) to distinguish between high- and low-metallicity branches, we find $\text{N2} > -1.0$ across the extent of SAMI609396B, prompting us to consider only the high-metallicity branch.

(iii) **O3N2:** Calibration based on large compilation of T_e measurements in H II regions from Marino et al. (2013).

(iv) **N2S2H α :** This diagnostic was proposed by Dopita et al. (2016) based on predictions from photoionization modelling. We adopt the calibration presented therein.

The colour maps shown in Fig. 6 are shown with different normalization so as to visualize any spatial trends in metallicity in each diagnostic, setting aside the expected discrepancies in normalization between alternative diagnostics (e.g. Kewley & Ellison 2008). Indeed, even after applying the Y20 correction, the median direct method metallicity ($\bar{Z}_{\text{Te}, \text{Y20}} = 8.40$) is still nearly 0.3 dex lower than that of the theoretically calibrated N2O2 diagnostic ($\bar{Z}_{\text{N2O2}} = 8.68$). This difference is consistent with previous work which has shown systematic offset between metallicities derived from N2O2 using theoretical and empirical calibrations (Bresolin et al. 2009; Bresolin & Kennicutt 2015).

4.3 Is the metallicity gradient positive or negative?

While it is widely known that different metallicity measurement techniques often disagree in normalization, one would hope that at a minimum two methods should agree on the ranked order of metallicities they measure. It is immediately striking from Fig. 6 that even qualitative spatial trends in metallicity are very sensitive to the adopted diagnostic. Fig. 7 illustrates these spatial trends as a 1D projection. Given the disturbed morphology of SAMI609396B, we do not formally define a metallicity gradient, but instead examine 1D

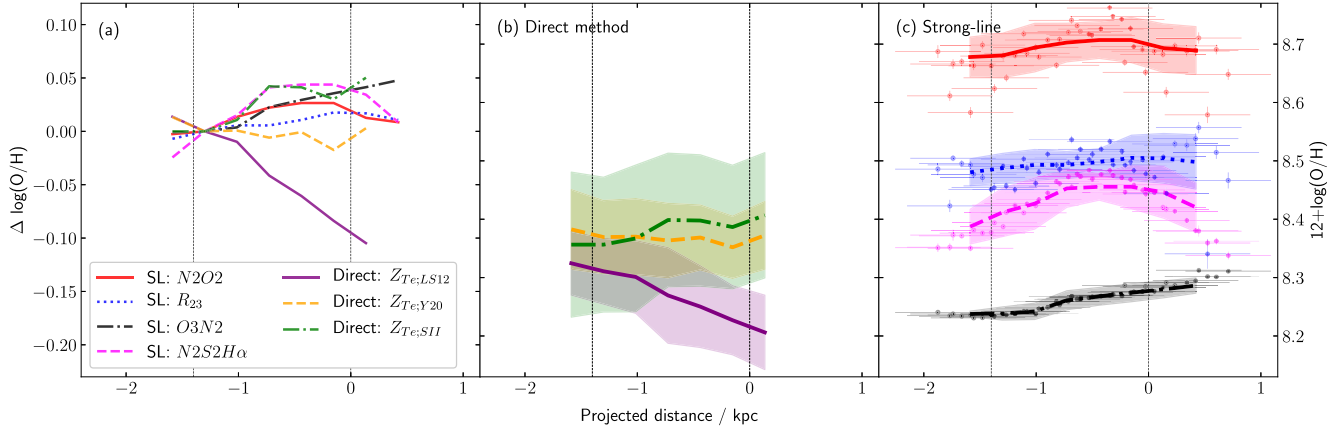


Figure 7. Spatial trend in metallicity along a mock slit for seven different strong-line and direct method metallicity measurement techniques. Panel (c) shows individual spaxels and running median trends measured with $N2O2$ (red), $O3N2$ (black), R_{23} (blue), and $N2S2H\alpha$ (magenta). Colour coding is as indicated in the legend in panel (a). More details on these strong-line metallicities can be found in Section 4.2. Panel (b) reproduces trend lines for three different direct method assumptions from Fig. 5 for ease of comparison. Panel (a) renormalizes each of these seven trend lines to show metallicity deviation. The horizontal axis is zeroed at the adopted core of SAMI609396B, taken as the location of the peak in i -band flux from SDSS imaging. The vertical error bars show the measurement uncertainty carrying through from emission line measurements. The horizontal error bars indicate the FWHM of the spatial PSF of the SAMI observation in terms of physical distance.

spatial trends along the mock slit shown in Figs 5(a)–(c) and Fig. 6(f). This slit encompasses the region of highest emission line signal to noise and approximately corresponds to the region of highest g -band flux (Fig. 1).

Panel (a) of Fig. 7 shows the running medians in metallicity with projected distance along this mock slit for all four strong-line methods described in Section 4.2 as well as the three different direct method assumptions outlined in Section 4.1. The distance axis has been zeroed at the location of peak i -band flux from SDSS imaging which we adopt as the core of SAMI609396B. Each trend line has been renormalized relative to the metallicity at $r = -1.3$ kpc. We renormalize at this projected distance rather than the core as the three direct method approaches show best agreement in this spatial region (Fig. 7b). In particular, the $Y20$ empirical corrections are smallest in this region.

Most striking in Fig. 7(a) is the clear discrepancy between the $Z_{Te,LS12}$ direct method and all other methods. The $Z_{Te,LS12}$ method favours a strong trend of decreasing metallicity left-to-right from negative projected distance toward the core. Strong-line methods show an opposite trend, with metallicity increasing in the same direction albeit with less overall deviation from uniform. As outlined in Section 4.1, we find that the $Z_{Te,Y20}$ and $Z_{Te,SII}$ direct methods both show a much flatter metallicity trend than the $Z_{Te,LS12}$ method, and are in better agreement with strong-line methods.

Given that strong-line methods have their own unsettled systematic uncertainties (Section 5.1), we do not assess the absolute correctness of ‘gradients’ derived from each method. Instead, we discuss below the physical reason for why the gradient from the $Z_{Te,LS12}$ method is at odds with $Z_{Te,Y20}$ and $Z_{Te,SII}$ and the strong line methods.

4.4 O^{2+}/O^{+} abundance ratio variation

We attribute the cause of the discrepancy between $Z_{Te,LS12}$ and other methods to variations in the O^{2+}/O^{+} abundance ratio, causing deviations from the fixed $T_e([O II]) - T_e([O III])$ relation adopted by $Z_{Te,LS12}$. Fig. 8 shows separate O^{+}/H^{+} and O^{2+}/H^{+} abundance maps, derived using $T_e([S II])$ and $T_e([O III])$ respectively, with panel (a) showing elevated O^{+}/H^{+} in the core region (lower-right;

corresponding to Projected Distance ≈ 0 kpc in horizontal scale of Fig. 7).

A bulk change in the ionization structure of H II regions across SAMI609396B such as this would cause measured temperatures to deviate from the $T_e([O II]) - T_e([O III])$ relation from López-Sánchez et al. (2012) (equation 6).⁵ In Section 3.3 we noted that $T_e([S II])$ and $T_e([O III])$ derived for two mock apertures indicated the absence of a strong positive correlation between $T_e([S II])$ and $T_e([O III])$ (Fig. 4 Panel e). In particular, lower $T_e([S II])$ values obtained in the core region leads to systematically higher O^{+} abundance measurements in $Z_{Te,SII}$ than $Z_{Te,LS12}$, driving the apparent reversal in the measured total oxygen abundance gradient.

Recently, Yates et al. (2020) observed that for $\log(O^{2+}/O^{+}) \lesssim 0.0$, ‘semidirect’ metallicities (that is, metallicities in which $T_e([O III])$ has been directly measured, but $T_e([O II])$ has been indirectly determined using an assumed $T_e([O II]) - T_e([O III])$ relation) underestimated the total metallicity by up to ~ 0.5 dex compared with metallicities derived using direct measurements of both $T_e([O II])$ and $T_e([O III])$. This effect also correlates with the $[O III]/[O II]$ strong-line ratio, motivating the $Y20$ correction for observations with $\log([O III]/\lambda\lambda 4959, 5007/[O II]\lambda\lambda 3726, 9) \leq 0.29$.

Fig. 8 shows that O^{2+}/O^{+} abundance ratios in SAMI609396B largely fall below $\log(O^{2+}/O^{+}) \lesssim 0.0$, inside the range highlighted in $Y20$ as giving rise to deficits in the total oxygen abundance when ‘semidirect’ methods are used. Furthermore, a spatial trend in O^{2+}/O^{+} abundance ratio can be seen in panel (c) of Fig. 8, with lower O^{2+}/O^{+} in the lower right regions of SAMI609396B. $Y20$ found that the ‘semidirect’ abundance deficit is more pronounced at lower values of O^{2+}/O^{+} . From this, we reason that it is likely that $Z_{Te,LS12}$ underestimates the total oxygen abundance across the majority of SAMI609396B. In particular, the lower O^{2+}/O^{+} seen in the core of SAMI609396B indicate that the systematically lower metallicities obtained in the core versus higher radius for $Z_{Te,LS12}$

⁵Or, indeed, any fixed monotonic relation assumed between $T_e([O II])$ and $T_e([O III])$.

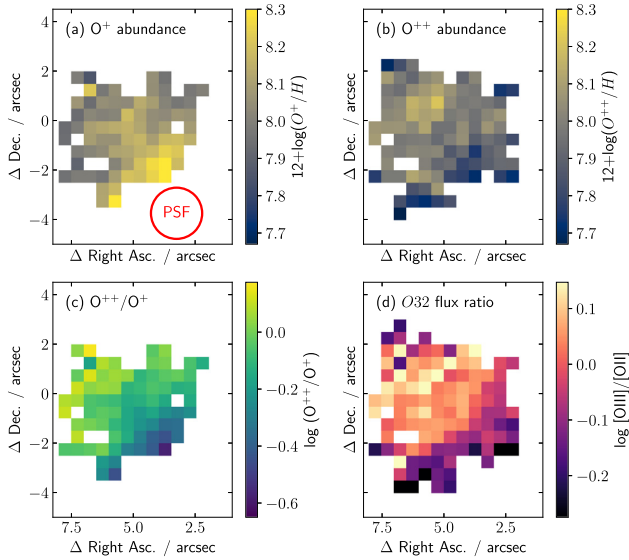


Figure 8. Map of derived O^{++}/O^{+} abundance ratio for SAMI609396B. (a) O^{+}/H^{+} abundance derived from equation (5) using $T_e[O II] = T_e[S II]$. (b) O^{++}/H^{+} abundance derived from equation (4) with direct $T_e[O III]$ measurement. Note that, unlike in Figs 5 and 7, abundance maps derived here use maps of $T_e[S II]$ and $T_e[O III]$ that have been smoothed by a Gaussian filter (FWHM set to measured PSF) to aid in the visual representation of spatial trends. (c) O^{++}/O^{+} abundance ratio. O^{+} provides a larger contribution to the total oxygen abundance across the majority of SAMI609396B ($\log(O^{++}/O^{+}) < 0$). Direct metallicities evaluated adopting an assumed $T_e[O II] - T_e[O III]$ relation (e.g. $Z_{Te,LS12}$ in this paper) can underestimate the total oxygen abundance by up to ~ 0.5 dex in this low ionization regime (see fig. 7 in Y20). (d) Observed O32 strong-line ratios (equation 9) appear to correlate with the O^{++}/O^{+} abundance ratio when O^{+}/H^{+} abundance is derived in this way. Regions of lowest O32 correspond to the highest level of correction according to Y20 correction (see Section 4.1.2).

(panel d of Fig. 5) can be explained by this semidirect abundance deficit being amplified in the core region.

By not appropriately accounting for this trend, when applying the $Z_{Te,LS12}$ method the O^{++}/O^{+} abundance ratio trend instead masquerades as the trend in total oxygen abundance seen in Figs 5 and 7.

5 DISCUSSION

5.1 Finer metallicity trends from strong lines

The measurement uncertainties on direct method metallicities for SAMI609396B are too large to be used for anything more than the bulk trend. While the strong-line methods show general agreement when considered in this bulk fashion, deviations exist in the finer details of their spatial trends (Figs 6 c–f and Fig. 7c). Most notable is the tendency of O3N2 to continue to increase beyond the core ($r > 0$ kpc in Fig. 7), out to the boundary of the star-formation selected region. While other strong line methods, especially N2S2H α and N2O2, favour a peak in metallicity around $r = -0.6$ kpc and decreasing past the core and beyond. We explore the possibility of this tension as arising from contaminating emission from non-star-forming sources below in Section 5.2.

5.2 Dissecting the emission line excitation mechanisms on the BPT diagram

Gas-phase metallicity studies such as this aim to determine abundances of nebulae photoionized by recently formed O- and B-type stars (H II regions). However, emission from other sources including active galactic nuclei (AGN), shock-heated gas (shocks), and diffuse ionized gas (DIG), may contribute significantly to an observed extragalactic emission spectrum. Since each of these sources exhibit characteristically different emission spectra, inference of the properties of ionized gas from an emission line spectrum requires knowledge (or an assumption) of the excitation mechanism causing the emission.

Different excitation sources are generally distinguished with BPT or VO87 diagnostic diagrams which compare $[O III]/H\beta$ to each of $[N II]/H\alpha$, $[S II]/H\alpha$, and $[O I]/H\alpha$ (Baldwin et al. 1981; Veilleux & Osterbrock 1987). Demarcation lines that separate H II regions from other sources of emission have been derived from photoionization modelling (Kewley et al. 2001) and from large samples of observational data (Kauffmann et al. 2003). These can be used to exclude observations which are dominated by emission sources other than H II regions.

Of course, the presence of one emission source in an observation does not preclude the presence of any others. Indeed a so-called ‘mixing sequence’ is often observed on diagnostic diagrams, spanning the regions between the loci inhabited by H II regions and those of other ionizing sources. Global spectra residing along this sequence are best explained as galaxies for which the global spectrum contains emission from both H II regions and either AGN or shocks, with the position along this mixing sequence determined by the relative proportion of each of these sources of emission. Further, when observations are made with IFU spectroscopy, mixing sequences can be spatially resolved within individual galaxies (Davies et al. 2014a, b, 2016, 2017; Ho et al. 2014; Jones et al. 2017; Zhang et al. 2017; D’Agostino et al. 2018) due to differing spatial distributions of emission sources within these galaxies.

Fig. 9 shows diagnostic line ratios for individual spaxels from SAMI DR2 single component emission line fits over the full extent of the SAMI609396 merger system. The purple points are those which pass the H II region Kewley et al. (2001) selection criteria in all three panels. The spatial region selected as SAMI609396B analysed in this paper is a subset of these purple points (refer to Fig. 2 for SAMI609396B spatial selection).

Overplotted on Fig. 9 are basis points predicted from photoionization modelling for H II regions (Dopita et al. 2013; green circles), fast shocks (Allen et al. 2008; blue triangle), and slow shocks (Dopita & Sutherland 2017; Sutherland & Dopita 2017; yellow inverted triangle) as well as observed loci of DIG-dominated regions (Sanders et al. 2017; Zhang et al. 2017; red star). The adopted model parameters for each of these basis points are summarized in Table 2. Note that the shock model basis points include a contribution from precursor emission. We assume a 50:50 contribution from the shock and precursor. H II region model parameters are based on metallicity and ionization parameter values obtained from N2O2 and O32 line ratios (see Section 4.2). Shock model parameters are difficult to constrain as they are degenerate with fractional contribution and spatial variations, not to mention the large modelling uncertainties. Selected shock velocities (Table 2) broadly reflect velocity dispersions observed in SAMI609396 (see Figs 2 and 10) and were chosen on the basis of how well they visually reproduced the individual points in Fig. 9. The black dashed lines show mixing models between H II regions and each of these other

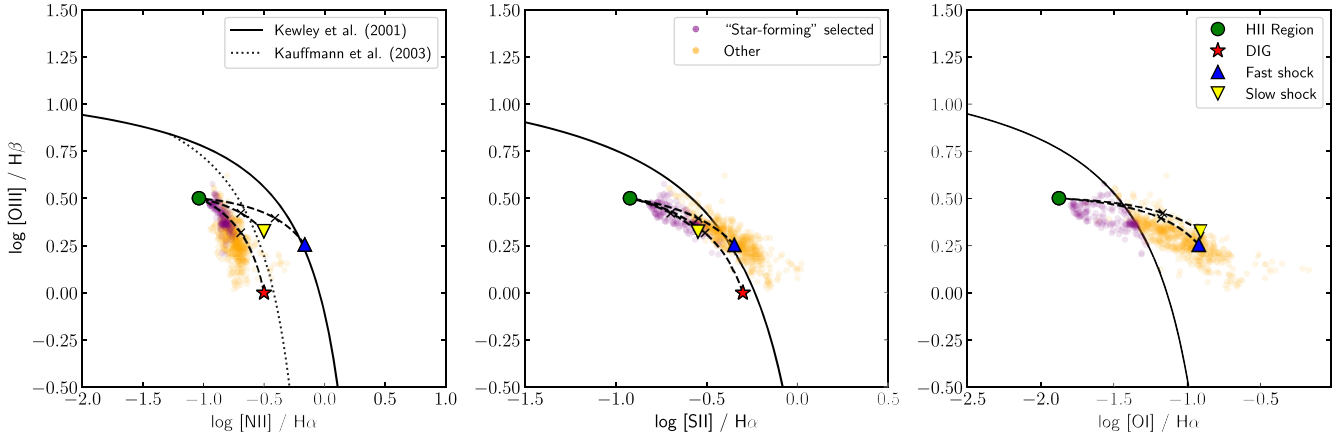


Figure 9. BPT & VO87 diagnostics diagrams for SAMI609396B. Line ratios for individual spaxels are shown as orange and purple points. Kewley et al. (2001) and Kauffmann et al. (2003) demarcation lines are shown as solid and dotted grey lines, respectively. The purple points denote spaxels below these demarcation lines in each panel. The solid shapes are basis points predicted from photoionization modelling for H II regions (Dopita et al. 2013; green circles), fast shocks (Allen et al. 2008; blue triangle) and slow shocks (Sutherland & Dopita 2017, Dopita & Sutherland 2017; yellow inverted triangle) according to the model parameters given in Table 2. The DIG basis point (red stars) is adopted as the peak region of strong-line ratios from the 10 per cent lowest surface brightness spaxels in the Zhang et al. (2017) MaNGA sample (Sanders et al. 2017). Black dashed lines indicate fractional mixing sequences between these basis points.

Table 2. Input parameters for basis points shown in Fig. 9.

		Z/Z_{\odot}	$\log(q)$	κ
H II region ^a		1.0	7.75	50
Fast shock ^{b, d}	v (km s ⁻¹)	Z/Z_{\odot}	n (cm ⁻³)	B (μG)
	250	1.0	10	10
Slow shock ^{c, d}		1.0	1000	6.1

Notes. ^aDopita et al. (2013); ^bAllen et al. (2008)

^cSutherland & Dopita (2017)

^dShock basis points include 50 per cent contribution from pre-cursor

emission sources. These lines indicate the sequence that arises by varying in the fractional contribution between the two fixed basis points. The mid-point of each sequence is labelled with a black cross.

In addition to emission line ratios, velocity dispersion is a useful tool for identifying the presence of shocks. Emission from shocks often shows a positive correlation between velocity dispersion and $[SII]/H\alpha$ or $[OI]/H\alpha$ diagnostic line ratios (Ho et al. 2014), while DIG emission will not yield such a correlation. In Fig. 10, $[SII]/H\alpha$ and $[OI]/H\alpha$ emission line ratios from SAMI609396 are plotted against measured velocity dispersion, supplementing our BPT and VO87 diagrams. Fig. 10 shows that both $[SII]/H\alpha$ and $[OI]/H\alpha$ ratios are positively correlated with velocity dispersion in SAMI609396. While emission line ratios alone cannot definitively distinguish between emission from shocks and DIG (Fig. 9), on the basis of Fig. 10 we conclude that the dominant source of non-star-forming emission observed in the SAMI609396 data cube is shock-heated gas.

5.2.1 Effect of contaminating emission

Given the limited (\sim kpc) spatial resolution of SAMI, some amount of contamination from non-star-forming emission sources is inevitable, despite limiting our analysis to the region of nominally star-forming dominated emission. Sanders et al. (2017) showed that contamination from DIG can lead to discrepancies in measured metallicity of up

to ~ 0.3 dex. In resolved studies, Poetrodjojo et al. (2019) found that the inclusion of DIG in metallicity gradient measurements affects all diagnostics to varying degrees.

Of particular concern to establish the robustness of gradient studies is the presence of significant systematic variation in the relative contribution of H II region and non-star-forming emission. This has the potential to affect the inference on spatial metallicity trends. Fig. 9 suggests that spaxels in this star-forming selected region may form the beginning of a spatial mixing sequence, perhaps indicating existence of spatial variations in the fractional contribution of shock emission to the total emission. Given the multiple ways metallicities from different diagnostics can be affected by contaminating emission, these variations could help to explain differences in the apparent metallicity trends recovered.

Line ratios plotted in Figs 9 and 10 support our assumption that the ‘star-forming’ selected spaxels associated with SAMI609396B are indeed dominated by emission from H II regions. However, it should be considered that even in regions with emission ‘dominated’ by H II regions, some amount of non-star-forming emission will invariably be present. In particular, the mixing sequences shown as black dashed lines in Fig. 9 highlight that there is room for variation in the relative contribution of different emission sources without moving outside the scope of what can be considered ‘dominated’ by H II regions. A quantitative assessment of this effect is beyond the scope of this paper, but we note that variable contributions of non-star-forming emission in IFU observations of galaxies has the potential to affect measured trends in gas-phase abundances.

In Section 4 we showed that, aside from the $Z_{Te, LS12}$ application of the direct method, our metallicity measurements favour a flattened metallicity gradient. This flat gradient is likely due to the effects of the merger, which are known to produce flattened metallicity gradients due to strong inflows of pristine galaxies from the outskirts of galaxies (e.g. Kewley et al. 2010). The measured gradient may be affected by the presence of shocks, however given that these metallicities were derived using a relatively small subset of the mixing sequence seen in Fig. 9 (i.e. the purple points) the effect of this contribution is likely not too significant.

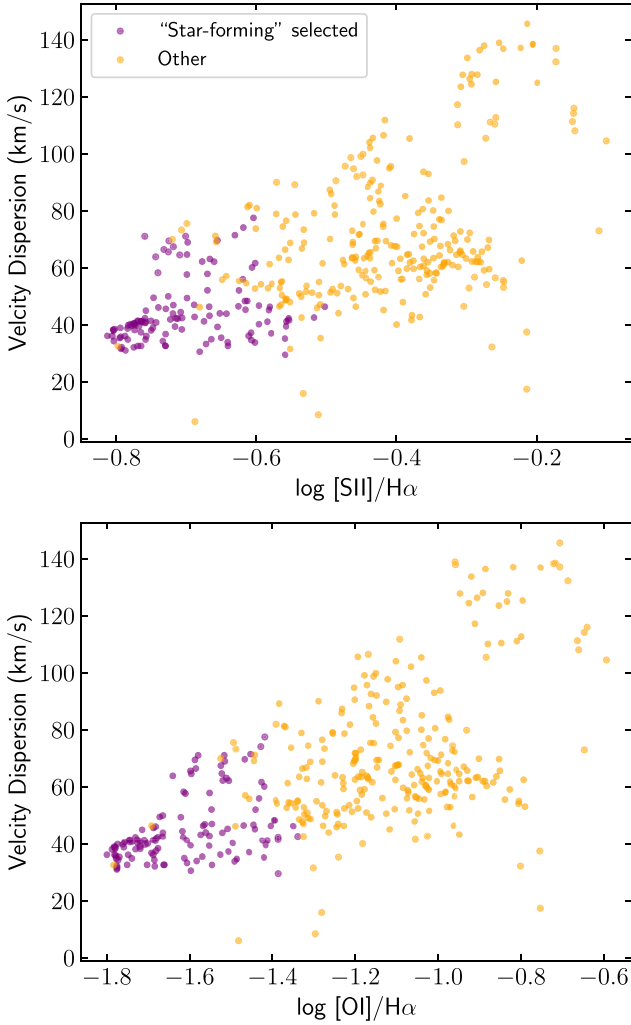


Figure 10. $[S II]/H\alpha$ and $[O I]/H\alpha$ diagnostic line ratios plotted against velocity dispersion for the full SAMI609396 field of view. The positive correlation observed between each of these diagnostic line ratios and velocity dispersion indicates the presence of shocks. The line ratio shown on the horizontal axis is $[S II]\lambda\lambda 6716, 31 / H\alpha$ for the top panel and $[O I]\lambda 6300 / H\alpha$ in the bottom panel. Colour coding is as for Fig. 9. Emission line fluxes and velocity dispersions shown in this figure are from 1-component fits provided in the SAMI DR2 value-added data products.

6 CONCLUSION

Following a search of the SAMI Galaxy Survey Data Release 2 Public Data, we identified SAMI609396B, an interacting galaxy showing high S/N , spatially-resolved detections of three auroral lines: $[O III]\lambda 4363$, $[S II]\lambda\lambda 4069, 76$ and $[S III]\lambda 6312$. The source also has properties that make it a good candidate for a local analogue of high redshift galaxies, in particular for its combination of moderate stellar mass, disturbed morphology, and elevated specific star formation rate (see Section 2.2 and Appendix B).

We use $[O III]$ and $[S II]$ auroral-to-strong line ratios to derive spatially resolved electron temperature measurements for two sub-regions within the emitting $H II$ regions ($T_e([O III])$ and $T_e([S II])$). Our results indicate the absence of a strong positive correlation between the $T_e([S II])$ and $T_e([O III])$ temperatures across different spatial regions in SAMI609396B. Instead, Fig. 4 shows $T_e([S II])$ and $T_e([O III])$ appearing to trend in opposite directions between two

apertures. This deviates from the common assumption of a fixed positive monotonic relation between these different temperatures.

Our $T_e([O III])$ measurements allow for direct method O^{2+}/H^+ abundance measurements. We then derive direct method total oxygen abundances under three different treatments of the O^+/H^+ abundance:

- (i) $Z_{Te, LS12}$: $T_e([O II])$ is assumed from $T_e([O II]) - T_e([O III])$ relation (López-Sánchez et al. 2012).
- (ii) $Z_{Te, Y20}$: As for $Z_{Te, LS12}$, with additional Y20 empirical correction, based on $[O III]/[O II]$ strong-line ratio.
- (iii) $Z_{Te, SII}$: $T_e([O II])$ adopted as $T_e([O II]) = T_e([S II])$.

We show that the disagreement between spatial metallicity trends returned by these methods is pronounced. $Z_{Te, LS12}$ favours a strong spatial trend with much lower total oxygen abundances being measured in the core, while $Z_{Te, Y20}$ and $Z_{Te, SII}$ instead suggest a flatter spatial trend, if anything perhaps opposite to the $Z_{Te, LS12}$ trend. We conclude that the cause of this disagreement is variation in the O^{2+}/O^+ abundance ratio causing deviations from the assumed $T_e([O II]) - T_e([O III])$ relation. Accordingly, $Z_{Te, LS12}$ results in systematically lower O^+ abundances across the whole of SAMI609396B than those of $Z_{Te, SII}$. This gives rise to an apparent metallicity gradient as the effect is not spatially uniform: O^+ abundance is particularly elevated in the core when probed by $Z_{Te, SII}$. The measured variation in the O^{2+}/O^+ abundance ratio correlates with variations in the $[O III]/[O II]$ strong line ratio. Thus, applying the empirical correction from Yates et al. (2020) ($Z_{Te, Y20}$) results in a trend more in line with $Z_{Te, SII}$. Additionally, we derive metallicity with four strong-line diagnostics (R_{23} , $N2O2$, $O3N2$, and $N2S2H\alpha$) using a mixture of observation- and theory-based calibrations. Spatial trends recovered by these strong-line methods again favour opposite trends to that of $Z_{Te, LS12}$, much more in line with those observed with $Z_{Te, SII}$ and $Z_{Te, Y20}$.

From diagnostic diagrams, we identify the presence of non-star-forming emission in the SAMI609396 system. We attribute this emission to shock-heated gas on the basis of the observed correlation between the $[S II]/H\alpha$ emission line ratio and the measured velocity dispersion. Despite applying our analysis to the star-forming selected region around SAMI609396B, we note that in reality each spaxel will contain some amount of contaminating, non-star-forming emission. In particular, we show that spaxels in this star-forming selected region appear to form the beginning of a spatial mixing sequence, indicating spatial variations in the fractional contribution of non-star-forming emission to the total emission. Given the different ways metallicities from different diagnostics can be affected by contaminating emission, these variations could help to explain differences in the apparent metallicity trends recovered.

Aside from the $Z_{Te, LS12}$ application of the direct method, our metallicity measurements favour a flat metallicity gradient for SAMI609396B. This flat gradient can be explained by the effects of the merger which are known to produce flattened metallicity gradients due to inflow of pristine gas from large radii (Kewley et al. 2010). However, possible contamination from shock emission may affect the gradient measurement.

The direct method remains the main calibration baseline for studying the chemical evolution of galaxies. However, it is not immune to modelling uncertainties. This study highlights the importance of adequately constraining the internal ionization and temperature structure within $H II$ regions when probing spatial variations of the metallicity across galaxies. We have shown here that abundance measurements based on $T_e([O III])$ alone are not a good indicator of

the metallicity gradient in SAMI609396B due to their sensitivity to the ionization parameter.

Spatially resolved applications of the direct method are currently limited even within the local Universe. Low-mass galaxies ($<10^{9.5} M_{\odot}$) contribute significantly to the stellar mass density and escape fraction of hydrogen ionizing photons at high redshift. However, the internal chemical distribution of these low-mass galaxies are rarely constrained owing to the spatial resolution and detection limit. This situation will be improved by forthcoming facilities such as *JWST*/NIRSpec and ground-based ELTs, which will push both the depth and spatial resolution attainable for IFU observations. In-depth analysis of local objects like SAMI609396B, thus set the stage for future detailed metallicity analysis of low-mass galaxies at high redshift.

ACKNOWLEDGEMENTS

We would like to thank Rob Yates for detailed discussions about the Yates et al. (2020) semidirect method and for sharing insights on using the O32 ratio to distinguish between lower and upper branch values in Fig. D1. We are grateful to Tucker Jones for valuable discussions about this work and to Jesse van de Sande and Ned Taylor for sharing SAMI-related expertise. We would also like to thank the referee for their constructive suggestions which certainly improved this work. This study was based on publicly released data from the SAMI Galaxy Survey. The SAMI Galaxy Survey is based on observations made at the Anglo-Australian Telescope. The Sydney-AAO Multi-object Integral field spectrograph (SAMI) was developed jointly by the University of Sydney and the Australian Astronomical Observatory. This research was supported by the Australian Research Council Centre of Excellence for All Sky Astrophysics in 3 Dimensions (ASTRO 3D), through project number CE170100013. AJC acknowledges support from an Australian Government Research Training Program (RTP) Scholarship.

DATA AVAILABILITY

This paper uses data from the SAMI Galaxy Survey Public Data Release 2 (Scott et al. 2018) which are available at <https://sami-survey.org/abdr>. Those data products include strong emission line flux maps; the auroral emission line flux maps used here are available from the corresponding author (AJC) on reasonable request. A list of SAMI galaxies identified in our search as showing auroral line emission is given in Appendix A.

REFERENCES

Allen M. G., Groves B. A., Dopita M. A., Sutherland R. S., Kewley L. J., 2008, *ApJS*, 178, 20
 Allen J. T. et al., 2015, *MNRAS*, 446, 1567
 Arellano-Córdova K. Z., Rodríguez M., 2020, *MNRAS*, 497, 672
 Baldwin J. A., Phillips M. M., Terlevich R., 1981, *PASP*, 93, 5
 Belfiore F. et al., 2017, *MNRAS*, 469, 151
 Berg D. A. et al., 2013, *ApJ*, 775, 128
 Berg D. A., Skillman E. D., Croxall K. V., Pogge R. W., Moustakas J., Johnson-Groh M., 2015, *ApJ*, 806, 16
 Berg D. A., Pogge R. W., Skillman E. D., Croxall K. V., Moustakas J., Rogers N. S. J., Sun J., 2020, *ApJ*, 893, 96
 Bian F., Kewley L. J., Dopita M. A., Juneau S., 2016, *ApJ*, 822, 62
 Bradley L. et al., 2019, *astropy/photutils*: v0.7.2. Available at: <https://doi.org/10.5281/zenodo.3568287>
 Bresolin F., 2019, *MNRAS*, 488, 3826
 Bresolin F., Kennicutt R. C., 2015, *MNRAS*, 454, 3664

Bresolin F., Garnett D. R., Kennicutt Robert C. Jr., 2004, *ApJ*, 615, 228
 Bresolin F., Ryan-Weber E., Kennicutt R. C., Goddard Q., 2009, *ApJ*, 695, 580
 Bryant J. J. et al., 2015, *MNRAS*, 447, 2857
 Bundy K. et al., 2015, *ApJ*, 798, 7
 Cappellari M., 2017, *MNRAS*, 466, 798
 Cappellari M., Verolme E. K., van der Marel R. P., Verdoes Kleijn G. A., Illingworth G. D., Franx M., Carollo C. M., de Zeeuw P. T., 2002, *ApJ*, 578, 787
 Cardamone C. et al., 2009, *MNRAS*, 399, 1191
 Cardelli J. A., Clayton G. C., Mathis J. S., 1989, *ApJ*, 345, 245
 Carton D. et al., 2018, *MNRAS*, 478, 4293
 Croom S. M. et al., 2012, *MNRAS*, 421, 872
 Croxall K. V., Pogge R. W., Berg D. A., Skillman E. D., Moustakas J., 2015, *ApJ*, 808, 42
 Croxall K. V., Pogge R. W., Berg D. A., Skillman E. D., Moustakas J., 2016, *ApJ*, 830, 4
 Curti M., Cresci G., Mannucci F., Marconi A., Maiolino R., Esposito S., 2017, *MNRAS*, 465, 1384
 Curti M., Mannucci F., Cresci G., Maiolino R., 2020a, *MNRAS*, 491, 944
 Curti M. et al., 2020b, *MNRAS*, 492, 821
 D'Agostino J. J., Poetrodjojo H., Ho I. T., Groves B., Kewley L., Madore B. F., Rich J., Seibert M., 2018, *MNRAS*, 479, 4907
 Davies R. L., Rich J. A., Kewley L. J., Dopita M. A., 2014a, *MNRAS*, 439, 3835
 Davies R. L., Kewley L. J., Ho I. T., Dopita M. A., 2014b, *MNRAS*, 444, 3961
 Davies R. L. et al., 2016, *MNRAS*, 462, 1616
 Davies R. L. et al., 2017, *MNRAS*, 470, 4974
 Deharveng L., Peña M., Caplan J., Costero R., 2000, *MNRAS*, 311, 329
 Dopita M. A., Sutherland R. S., 2017, *ApJS*, 229, 35
 Dopita M. A., Sutherland R. S., Nicholls D. C., Kewley L. J., Vogt F. P. A., 2013, *ApJS*, 208, 10
 Dopita M. A., Kewley L. J., Sutherland R. S., Nicholls D. C., 2016, *Ap&SS*, 361, 61
 Edmunds M. G., Greenhow R. M., 1995, *MNRAS*, 272, 241
 Finlator K., 2017, in Fox A. J., Davé R., eds, *Gas Accretion and Galactic Chemical Evolution: Theory and Observations*. Springer, p. 221
 Green A. W. et al., 2014, *MNRAS*, 437, 1070
 Green A. W. et al., 2018, *MNRAS*, 475, 716
 Heckman T. M. et al., 2005, *ApJ*, 619, L35
 Hemler Z. S. et al., 2020, preprint ([arXiv:2007.10993](https://arxiv.org/abs/2007.10993))
 Ho I. T. et al., 2014, *MNRAS*, 444, 3894
 Ho I. T., Kudritzki R.-P., Kewley L. J., Zahid H. J., Dopita M. A., Bresolin F., Rupke D. S. N., 2015, *MNRAS*, 448, 2030
 Ho I. T. et al., 2019, *ApJ*, 885, L31
 Izotov Y. I., Stasińska G., Meynet G., Guseva N. G., Thuan T. X., 2006, *A&A*, 448, 955
 Jones A. et al., 2017, *A&A*, 599, A141
 Jones T., Ellis R. S., Richard J., Jullo E., 2013, *ApJ*, 765, 48
 Jones T., Sanders R., Roberts-Borsani G., Ellis R. S., Laporte N., Treu T., Harikane Y., 2020, *ApJ*, 903, 150
 Kauffmann G. et al., 2003, *MNRAS*, 346, 1055
 Kewley L. J., Dopita M. A., 2002, *ApJS*, 142, 35
 Kewley L. J., Ellison S. L., 2008, *ApJ*, 681, 1183
 Kewley L. J., Dopita M. A., Sutherland R. S., Heisler C. A., Trevena J., 2001, *ApJ*, 556, 121
 Kewley L. J., Groves B., Kauffmann G., Heckman T., 2006, *MNRAS*, 372, 961
 Kewley L. J., Rupke D., Zahid H. J., Geller M. J., Barton E. J., 2010, *ApJ*, 721, L48
 Kewley L. J., Maier C., Yabe K., Ohta K., Akiyama M., Dopita M. A., Yuan T., 2013, *ApJ*, 774, L10
 Kewley L. J., Nicholls D. C., Sutherland R. S., 2019, *ARA&A*, 57, 511
 Kobulnicky H. A., Kewley L. J., 2004, *ApJ*, 617, 240
 Leethochawalit N., Jones T. A., Ellis R. S., Stark D. P., Richard J., Zittrn A., Auger M., 2016, *ApJ*, 820, 84
 Li Y., Bresolin F., Kennicutt Robert C. J., 2013, *ApJ*, 766, 17

López-Sánchez Á. R., Dopita M. A., Kewley L. J., Zahid H. J., Nicholls D. C., Scharwächter J., 2012, *MNRAS*, 426, 2630

Luridiana V., Morisset C., Shaw R. A., 2015, *A&A*, 573, A42

Ma X., Hopkins P. F., Feldmann R., Torrey P., Faucher-Giguère C.-A., Kereš D., 2017, *MNRAS*, 466, 4780

Magrini L., Coccato L., Stanghellini L., Casasola V., Galli D., 2016, *A&A*, 588, A91

Maiolino R., Mannucci F., 2019, *A&AR*, 27, 3

Marino R. A. et al., 2013, *A&A*, 559, A114

Medling A. M. et al., 2018, *MNRAS*, 475, 5194

Morales-Luis A. B., Pérez-Montero E., Sánchez Almeida J., Muñoz-Tuñón C., 2014, *ApJ*, 797, 81

Moustakas J., Kennicutt, Robert C. J., Tremonti C. A., Dale D. A., Smith J.-D. T., Calzetti D., 2010, *ApJS*, 190, 233

Nicholls D. C., Dopita M. A., Sutherland R. S., Jerjen H., Kewley L. J., Basurrah H., 2014, *ApJ*, 786, 155

Nicholls D. C., Kewley L. J., Sutherland R. S., 2020, *PASP*, 132, 033001

Oke J. B., Gunn J. E., 1983, *ApJ*, 266, 713

Peimbert M., 1967, *ApJ*, 150, 825

Peimbert M., Peimbert A., Delgado-Inglada G., 2017, *PASP*, 129, 082001

Pérez-Montero E., 2017, *PASP*, 129, 043001

Pettini M., Pagel B. E. J., 2004, *MNRAS*, 348, L59

Pilyugin L. S., Thuan T. X., 2005, *ApJ*, 631, 231

Planck Collaboration XIII, 2016, *A&A*, 594, A1

Poetrodjojo H. et al., 2018, *MNRAS*, 479, 5235

Poetrodjojo H., D’Agostino J. J., Groves B., Kewley L., Ho I. T., Rich J., Madore B. F., Seibert M., 2019, *MNRAS*, 487, 79

Proxauf B., Öttl S., Kimeswenger S., 2014, *A&A*, 561, A10

Renzini A., Peng Y.-j., 2015, *ApJ*, 801, L29

Sánchez S. F. et al., 2012, *A&A*, 538, A8

Sanders R. L. et al., 2016, *ApJ*, 816, 23

Sanders R. L., Shapley A. E., Zhang K., Yan R., 2017, *ApJ*, 850, 136

Sanders R. L. et al., 2020, preprint ([arXiv:2009.07292](https://arxiv.org/abs/2009.07292))

Scott N. et al., 2018, *MNRAS*, 481, 2299

Searle L., 1971, *ApJ*, 168, 327

Sharp R. et al., 2015, *MNRAS*, 446, 1551

Speagle J. S., Steinhardt C. L., Capak P. L., Silverman J. D., 2014, *ApJS*, 214, 15

Steidel C. C. et al., 2014, *ApJ*, 795, 165

Sutherland R. S., Dopita M. A., 2017, *ApJS*, 229, 34

Taylor E. N. et al., 2011, *MNRAS*, 418, 1587

Tissera P. B., Rosas-Guevara Y., Bower R. G., Crain R. A., del P Lagos C., Schaller M., Schaye J., Theuns T., 2019, *MNRAS*, 482, 2208

Torrey P., Cox T. J., Kewley L., Hernquist L., 2012, *ApJ*, 746, 108

Vazdekis A., Sánchez-Blázquez P., Falcón-Barroso J., Cenarro A. J., Beasley M. A., Cardiel N., Gorgas J., Peletier R. F., 2010, *MNRAS*, 404, 1639

Veilleux S., Osterbrock D. E., 1987, *ApJS*, 63, 295

Vila-Costas M. B., Edmunds M. G., 1992, *MNRAS*, 259, 121

Wang X. et al., 2020, *ApJ*, 900, 183

Yates R. M., Schady P., Chen T. W., Schweyer T., Wiseman P., 2020, *A&A*, 634, A107

Yuan T. T., Kewley L. J., Swinbank A. M., Richard J., Livermore R. C., 2011, *ApJ*, 732, L14

Yuan T. et al., 2020, *Nat. Astron.*, 4, 957

Zahid H. J., Geller M. J., Kewley L. J., Hwang H. S., Fabricant D. G., Kurtz M. J., 2013, *ApJ*, 771, L19

Zhang K. et al., 2017, *MNRAS*, 466, 3217

Zhou L. et al., 2017, *MNRAS*, 470, 4573

APPENDIX A: SAMI GALAXIES WITH AURORAL LINES

We provide in Table A1 a list of galaxies in SAMI Data Release 2 public data showing visually identifiable [O III] $\lambda 4363$ emission. We do not claim that this list is exhaustive; rather, it is intended to provide a starting point for any future work hoping to make use of auroral line detections in SAMI data. This list was compiled

Table A1. SAMI Galaxies with visually identifiable [O III] $\lambda 4363$ emission.

SAMI ID
84107
137071
177518
209319
325376
561143
567676
567736
609396

during an exploratory search of the SAMI Data Release public data by visually inspecting the 1D spectra obtained by binning spaxels with the highest signal-to-noise on the H α emission line. All cases other than SAMI609396 required some degree of spatial binning to achieve $S/N_{\lambda 4363} \gtrsim 5$. In our brief exploration we found that typically fewer than ~ 4 –5 usable bins could be extracted, however we did not expend any effort optimizing these binning schemes. Our search focused on the [O III] $\lambda 4363$ auroral line, however we note that in many of the galaxies listed in Table A1, [S II] $\lambda \lambda 4069, 76$ and [S III] $\lambda 6312$ are also clearly present. We speculate that there may be galaxies with prominent [S II] and [S III] auroral line emission which were not picked up in our [O III] based search. We note that the [N II] $\lambda 5755$ and [O II] $\lambda \lambda 7320, 30$ auroral lines are typically not observable with SAMI. The [N II] $\lambda 5755$ auroral line falls in the wavelength gap between the blue and red arms in the SAMI datacubes. The [O II] $\lambda \lambda 7320, 30$ line falls near the red limit of the SAMI Galaxy Survey data and often outside the spectral coverage. Even in cases where it falls inside the spectral coverage, we find it is not detectable.

APPENDIX B: GLOBAL PROPERTIES

SAMI DR2 value added data products include a spatially resolved star-formation rate (SFR) map based on measured H α flux (refer to Medling et al. 2018 for details). We derive a global SFR for SAMI609396B by summing the spaxel by spaxel star-formation rate over the SAMI609396B selection mask defined in Section 2.2, obtaining $SFR = 4.21 \pm 0.30 M_{\odot} \text{ yr}^{-1}$. However, it is worth noting that the spatial region considered here is limited by the SAMI field-of-view which does not achieve full coverage of SAMI609396B (see Fig. 1). Indeed, the star-formation rate map (Fig. 2c) appears to peak near the FoV boundary. It is likely that the region extending beyond the FoV contributes significantly to the global SFR of SAMI609396B. In that sense, we suggest that the quoted SFR can be considered as a lower-bound. In addition to SAMI609396B, we derive SFR for the more massive companion galaxy by summing the SFR map over the remainder of the SAMI FoV. This yields a value of $SFR = 0.32 \pm 0.08 M_{\odot} \text{ yr}^{-1}$, although we note that this spatial region exhibits significant contribution to its emission spectrum from non-star-forming sources which may bias this value (Section 5.2).

We derive global stellar mass values from g - and i -band photometry using the relation described in Section 4.2 of Bryant et al. (2015), based on stellar mass estimates from Taylor et al. (2011). We create a deblended segmentation map for the SDSS g -band imaging using `detect_sources` and `deblend_sources` from `photutils` package (Bradley et al. 2019). We use default values of 32 multithresholding levels and a blending contrast of 0.001 to run the deblending. The magnitudes obtained from these segmentation images are given in Table B1. Applying the Bryant et al. (2015)

Table B1. Deblended magnitudes used to estimate stellar masses for SAMI609396B and companion.

	<i>g</i> -band	<i>i</i> -band
SAMI609396B	15.017 ± 0.001	14.932 ± 0.001
Companion	15.064 ± 0.001	14.351 ± 0.001

relation to those magnitudes we obtain stellar mass estimates of $\log(M_*/M_\odot) = 9.11 \pm 0.10$ for SAMI609396B and $\log(M_*/M_\odot) = 9.78 \pm 0.10$ for its more massive companion. The 0.10 dex uncertainties reflect the quoted $1\text{-}\sigma$ scatter in this relation (Taylor et al. 2011). We ignore the flux uncertainties from the SDSS imaging as these contribute only 0.001 dex variations in stellar mass. These values correspond to a mass ratio of ~ 0.21 for this merger system. The global SFR and M_* values derived here place SAMI609396B at least 1.3 dex above the star-forming main sequence (SFMS) for local star-forming galaxies (Renzini & Peng 2015).

APPENDIX C: SPECTRAL FITTING

The SAMI DR2 value-added release includes emission line maps for the most widely used strong optical lines. However, the primary focus of this work is the auroral emission lines, which are not included in these data products. Here we outline the methods behind our own spectral fitting to the SAMI DR2 data cubes. Flux measurements obtained here are used throughout Sections 3 and 4.

C1 Continuum subtraction

For each spaxel in the reduced SAMI datacube, we fit the stellar continuum of the blue and red arms simultaneously using pPXF (Cappellari 2017). The 1D spectra for each spaxel are logarithmically rebinned. Given the different wavelength resolutions of the two arms, the higher resolution red arm is sampled down to match the velocity scale of the lower spectral resolution blue arm. Four moment fits are performed to the stellar continuum using the MILES library of stellar templates (Vazdekis et al. 2010). Two moment fits to the Balmer emission lines and strongest forbidden emission lines ([O III] $\lambda\lambda 4959, 5007$, [N II] $\lambda\lambda 6548, 83$ and [S II] $\lambda\lambda 6716, 31$) are included in the fitting procedure, however these derived emission line fluxes are discarded (refer to Section C2 for emission line fitting).

SAMI609396 exhibits strong emission lines with high equivalent widths ($> 200 \text{ \AA}$) and thus even spectra from individual spaxels feature many faint emission lines that are not widely studied. To ensure that the effect of these faint emission lines on the stellar template fitting is minimized, an iterative sigma-clipping method is employed (described in Section 2.1 of Cappellari et al. 2002). In this approach, once a global minimum is found, spectral pixels deviating more than 3σ from this best-fitting template are masked out and a new global fit is obtained. This process is repeated until no additional pixels are masked out. As a final step, the fits were visually inspected to ensure no spurious spectral features affected the fitting.

A continuum subtracted spectrum was obtained for each spaxel by subtracting the best-fitting stellar spectrum from the reduced observed spectrum from the SAMI data cube.

C2 Emission-line fitting

Emission-line maps of the most commonly used strong emission lines are provided in the value-added SAMI public release data. However,

to ensure our emission-line ratios are making self-consistent comparisons between strong-lines and the faint auroral lines, we perform new fits to these strong lines as well as the auroral lines. The emission line fitting procedure applied to each spaxel is as follows.

We first fit the H α emission with a two-component Gaussian profile. We perform a χ^2 -minimization fit across the 6672–6698 Å wavelength range (rest-frame 6553–6578 Å at SAMI609396B catalogue redshift). This range encompasses > 99 per cent of the H α emission for the redshift range covered by the spaxels of this object while minimizing contribution from nearby [N II] emission lines. The H α emission is well modelled as a primary narrow component (median $\text{FWHM}_{\text{H}\alpha, \text{nar}} = 2.26 \text{ \AA}$, median redshift $z_{\text{nar}} = 0.018566$) and a secondary broad component (median $\text{FWHM}_{\text{H}\alpha, \text{brd}} = 7.07 \text{ \AA}$, median redshift $z_{\text{brd}} = 0.018493$) across the spatial extent of SAMI609396B.

We then fix the velocity and velocity dispersion for each of these two kinematic components to values obtained from H α and simultaneously fit across the full optical wavelength range for broad- and narrow-component fluxes for each of the strong emission lines ([O II] $\lambda\lambda 3726, 9$, H β , [O III] $\lambda\lambda 4959, 5007$, [O I] $\lambda 6300$, [N II] $\lambda\lambda 6548, 83$, H α , [S II] $\lambda 6716$, and [S II] $\lambda 6731$).

The flux of each of these components is allowed to vary freely above a lower bound of $f_{\text{comp}} \geq 0$ with the exception of [O III] $\lambda 4959$ and [N II] $\lambda 6548$. The fluxes of each component of these lines are tied to the flux of the corresponding component of [O III] $\lambda 5007$ and [N II] $\lambda 6583$, respectively, according to following theoretical ratios: $f_{5007} = 3 \times f_{4959}$ and $f_{6583} = 2.9 \times f_{6548}$.

We calculate the uncertainty in the flux for each component by adding in quadrature the statistical error from the fit to an estimate of the uncertainty in the level of the continuum. This continuum uncertainty term is calculated as $\sigma_l = \sigma_c \cdot \sqrt{N + EW/\Delta}$ (equation 1 in Pérez-Montero 2017) where σ_c is the standard deviation in a 30 Å range near the emission line, selected to contain only continuum flux, N is the number of spectral pixels encompassed by the fit Gaussian, EW is the equivalent width of the line, and Δ is the spectral dispersion (\AA pixel^{-1}). When considering the ‘total’ emission (i.e. sum of both components), the adopted uncertainty is the uncertainty of both components summed in quadrature.

With the exception of [O I] $\lambda 6300$, the faintest of these ‘strong-lines’, the fits to these strong lines achieve summed component $S/N > 20$ across the entire spatial extent of interest and achieve $S/N > 50$ in over 95 per cent of the spaxels. The [O I] $\lambda 6300$ line fits achieve $S/N > 20$ in > 95 per cent of spaxels but only $S/N > 50$ in the brightest 8 spaxels. These two-component fits were visually inspected, adding confidence to the automated algorithms.

The fainter emission lines do not present with sufficient signal to noise to be reliably modelled with two-component fits. Instead, to these fainter lines we make single component fits where the velocity and velocity dispersion are fixed to those derived for the dominant narrow component above. The faint lines for which single components are used include the three auroral emission lines visually identified to be present ([S II] $\lambda\lambda 4069, 76$, [O III] $\lambda 4363$, and [S III] $\lambda 6312$), and the fainter Balmer emission lines H δ and H γ . Additionally, we include the [Fe II] $\lambda 4360$ emission line in our single component fit. The effect of the presence of this blended emission feature on the measured [O III] flux is discussed in detail in Section C3.

As before, these emission line fluxes are allowed to vary freely with constraint of $f \geq 0$ except that fluxes of the [S II] $\lambda\lambda 4069, 76$ doublet are constrained such that $f_{4069} = 3 \times f_{4076}$. Uncertainties for each line are calculated in the same way as described for the individual components of the strong line fits described above. Once derived for each spaxel, these emission line fluxes are collated into

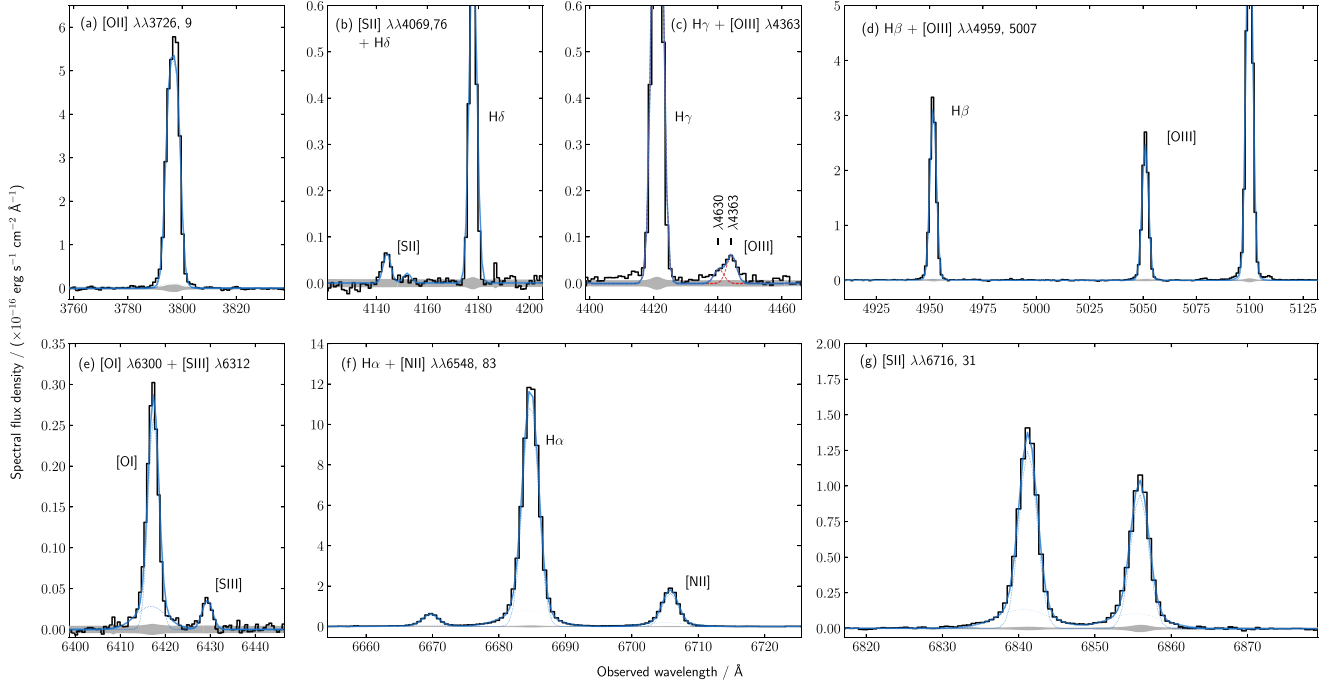


Figure C1. Emission line fits to a 1D spectrum from an individual spaxel. Each panels (a)–(g) highlights different emission lines used in this analysis as described in the inset text. Units on each axis are the same for each panel, however note the normalization on the vertical axis varies according to the strength of the emission lines shown. In each panel the continuum subtracted spectrum is shown as the black step plot, while the grey shaded band shows the $1\text{-}\sigma$ error spectrum. The best-fitting emission line model is shown by the solid blue line, while the blue dotted lines show the individual broad- and narrow-components fit to the profile, where applicable. The three auroral lines observed in SAMI609396B, [S II] $\lambda\lambda$ 4069, 76, [O III] λ 4363, and [S III] λ 6312, are shown in panels (b), (c), and (e), respectively. The red dashed lines in panel (c) show the individual profiles of the [Fe II] λ 4360 and [O III] λ 4363 emission lines, fit simultaneously to account for blending of these features (see Section C3).

2D maps. Emission line fits for an example 1D spaxel spectrum are shown in Fig. C1.

As a final step, we correct these 2D emission line flux maps using values from the extinction correction map provided in the SAMI DR2 data, derived using spatially smoothed Balmer decrements ($f_{\text{H}\alpha}/f_{\text{H}\beta}$) to account for aliasing effects introduced by the SAMI observing process (refer to Green et al. 2018 and Medling et al. 2018 for details), assuming a Cardelli, Clayton & Mathis (1989) extinction law with $R_V = 3.1$. Unless otherwise specified, the analysis of this paper is conducted using these reddening corrected emission line flux maps.

C3 [Fe II] λ 4360 & [O III] λ 4363 blending

Several recent studies have identified an emission feature at λ 4360 Å which may be blended with the [O III] λ 4363 emission line, attributed to an [Fe II] emission line (Curti et al. 2017; Berg et al. 2020; Arellano-Córdova & Rodríguez 2020). From visual inspection of 1D spectra, we identify that [O III] λ 4363 emission often presents with an extended blue wing, which we attribute to blending with this [Fe II] λ 4360 line.

We account for this by including an emission feature at this wavelength in our line-fitting routine whose flux is allowed to vary freely (Appendix C2). As with all faint lines in the line-fitting, the velocity and velocity dispersion is tied to that of the narrow component identified for H α . Visually, the fits obtained appear to model the emission features around λ 4363 Å well. The median ratio between the [O III] and [Fe II] lines across the spatial extent with $S/N_{\lambda 4363} > 3$ is $f_{4363}/f_{4360} = 2.1$ with standard deviation $\sigma_{4363/4360} = 1.47$.

As a check of how reliable our [O III] flux measurements with this blended [Fe II] + [O III] profile are, we fit this wavelength region using three approaches and compare the results. The three approaches are:

- (i) *Standard fitting*: As described in Appendix C2 where [Fe II] and [O III] components are simultaneously fit for.
 - (ii) *Naive single component*: A simple single component fit to [O III] across the wavelength range from 4345–4380 Å. No attempt is made to account for [Fe II] emission.
 - (iii) *Red wing single component*: A single component is fit to [O III], excluding pixels bluewards of $\lambda = 4362.5 \times (1 + z_{\text{fit}})$ Å, where z_{fit} is the redshift value obtained from the narrow-component fit to H α for the spaxel in question. This should mask out spectral pixels with > 5 per cent contribution from [Fe II] emission.
- In each approach, the velocity and velocity dispersion values are fixed to those obtained for the H α narrow component, as in our standard fitting. The best-fitting profiles from each of these approaches are shown in the top panel of Fig. C2. The bottom panel shows the distribution of values obtained for $f_{\text{alt}}/f_{\text{std}}$ ratios, where f_{std} is the [O III] flux obtained from method (i) and f_{alt} is the flux from approaches (ii) and (iii). As expected, when no attempt is made to account for [Fe II] emission as in method (ii), the [O III] flux is systematically overestimated by around 10 per cent ($f_{\text{alt}}/f_{\text{std}} = 1.09 \pm 0.04$; orange dash-dotted line in bottom panel of Fig. C2). However, when applying method (iii), where the blue wing of [O III] is masked out, we see no significant systematic offset from our values obtained by method (i) ($f_{\text{alt}}/f_{\text{std}} = 0.99 \pm 0.07$; purple dashed line in bottom panel of Fig. C2). We note that there is large scatter in the distribution of $f_{\text{alt}}/f_{\text{std}}$ for this latter case. This uncertainty of >10 per cent is not

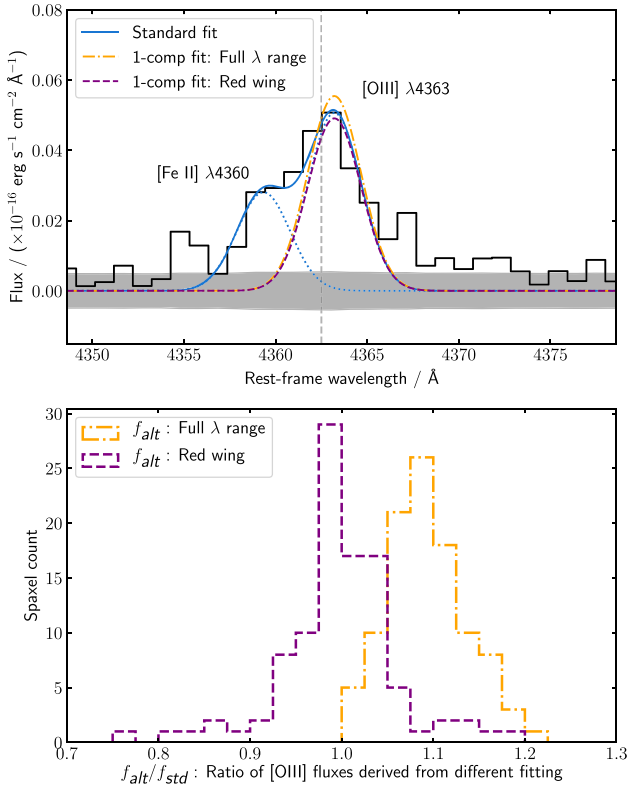


Figure C2. Top panel: example of fits obtained to the region around rest-frame $\lambda 4363$ when three different fitting methods are implemented. These methods are described in Appendix C3. Method (i) is shown by the blue solid line, with dotted lines showing each component. Method (ii) is shown by the orange dash-dotted line, while method (iii) is shown as the purple dashed line. The wavelength range used for method (iii) is that red-ward of 4362.5 \AA (denoted by vertical dashed line). Bottom panel: Histogram of spaxels with $S/N_{\lambda 4363} > 3$ of [O III] flux measurements obtained from methods (ii) and (iii), shown relative to [O III] flux obtained from method (i). As expected, when [Fe II] emission is not accounted for as in (ii), [O III] flux is systematically higher. While methods (iii) and (i) do not universally agree, the lack of systematic offset gives us confidence that either of these methods on average reliably account for [Fe II] emission.

unreasonable for observations with $S/N \sim 3\text{--}15$. We note also that when using these auroral line fluxes to derive electron temperature measurements, measurement uncertainties of this level are likely outweighed by modelling uncertainties (refer to Section 3).

From this we conclude that for the [O III]/[Fe II] flux ratios we observe ($f_{4363}/f_{4360} \sim 2.1$), on average methods (i) and (iii) each suffer minimally from contamination by this blended emission feature at $\lambda 4360$. [O III] $\lambda 4363$ flux measurements quoted in other sections are those derived from the standard fitting routine (method (i)).

APPENDIX D: IMPLEMENTING THE METHOD OF YATES ET AL. (2020)

Measurements of electron temperature (T_e) are highly sought after in chemical abundance studies as they enable ‘direct-method’ metallicity measurements to be made. Full application of the direct method to determine the total oxygen abundance requires measurements of both $T_e(\text{[O III]})$ and $T_e(\text{[O II]})$, such that both O^{2+}/H^+ and O^+/H^+ can be determined. However, given the faintness of the required auroral emission lines, often only $T_e(\text{[O III]})$ can be measured directly. In this

case, it is common to apply a ‘semidirect’ method. In this approach, the $T_e(\text{[O II]})$ is indirectly determined from the measured $T_e(\text{[O III]})$ via some assumed relation, allowing the O^+ abundance to be derived.

While it is common to assume a simple positive correlation between $T_e(\text{[O II]})$ and $T_e(\text{[O III]})$ (e.g. Izotov et al. 2006; López-Sánchez et al. 2012), Yates et al. (2020) (Y20 hereafter) find that this does a poor job of describing the observed scatter about this relation. Instead, Y20 highlight that at fixed metallicity, $T_e(\text{[O II]})$ is anticorrelated with $T_e(\text{[O III]})$, and that the general positive trend between $T_e(\text{[O II]})$ and $T_e(\text{[O III]})$ is due to the fact that both correlate negatively with metallicity and in general will both be higher in lower metallicity systems.

Based on these observations, Yates et al. (2020) have outlined a new method for determining $T_e(\text{[O II]})$ and metallicity in systems where only $T_e(\text{[O III]})$ can be directly measured. Unlike previous semidirect methods, in the Y20 method, $T_e(\text{[O II]})$ and metallicity are solved for simultaneously. This differs from previous semidirect methods in which $T_e(\text{[O II]})$ is usually determined based on $T_e(\text{[O III]})$ independently of metallicity. Metallicity is then subsequently determined using the value obtained for $T_e(\text{[O II]})$.

We note that this method (‘Y20 method’) is separate to the empirical correction described in that same publication which we performed in Section 4.1.2 (‘Y20 correction’), and the Y20 empirical correction still needs to be applied to the metallicities arising from the Y20 method.

In Section 4 we applied a simple semidirect method to our SAMI609396B data in which $T_e(\text{[O II]})$ was determined from $T_e(\text{[O III]})$ using the calibration of López-Sánchez et al. (2012) (equation 6 in Section 4.1) and then the metallicity subsequently determined accordingly (that method was referred to as $Z_{\text{Te;LS12}}$ throughout this work). Here, we additionally apply the Y20 method to our SAMI609396B data. We find the results of the Y20 method to be double-valued (Fig. D1). The ‘upper branch’ largely agrees with our $Z_{\text{Te;LS12}}$ metallicities within ~ 0.15 dex (median absolute offset is 0.06 dex), however the ‘lower branch’ gives starkly different values. Spatial metallicity trends arising from each branch of this method differ noticeably (Fig. D2), making it difficult to draw conclusions without further characterization of the behaviour of each branch in a larger data set. We describe the details of our implementation of the Y20 method below.

D1 Basis of the Yates method

The Y20 method differs from other semidirect methods in that $T_e(\text{[O II]})$ and metallicity (Z_{Te}) are evaluated simultaneously in order to account for the interdependence of these parameters at fixed $T_e(\text{[O III]})$, whereas typically semidirect methods have involved inferring a $T_e(\text{[O II]})$ value from a $T_e(\text{[O III]})$ measurement via a fixed relation and then subsequently determining the metallicity using this value.

The Y20 method centres on a metallicity-dependent fit to the $T_e(\text{[O II]}) - T_e(\text{[O III]})$ relation, outlined as follows:

$$T_e(\text{[O II]}) = \frac{a(Z_{\text{Te}})^2}{2 \cdot T_e(\text{[O III]})}, \quad (\text{D1})$$

where

$$a = -12030.22 \cdot Z_{\text{Te}} + 113720.75. \quad (\text{D2})$$

This can be solved simultaneously with the following equations which determine oxygen abundance from measured [O II]/H β and

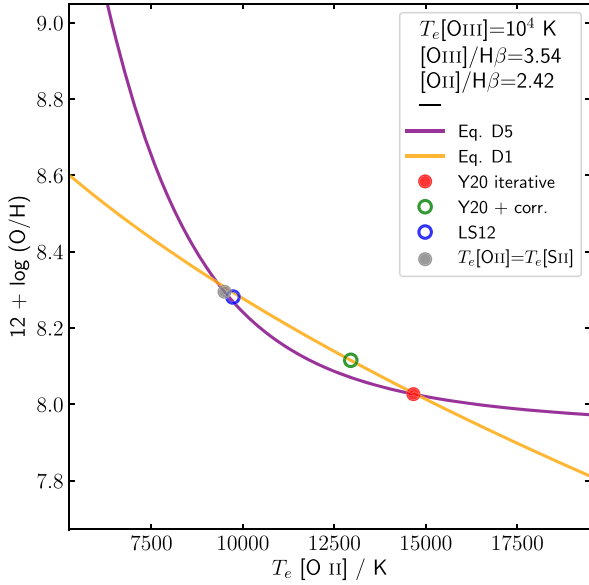


Figure D1. Solving for the intersection of equations D1 and D5 from the Y20 method yields two solutions: an ‘upper-branch’ solution on the left-hand side with a high metallicity, and a ‘lower-branch’ value on the right-hand side with a low metallicity. Here, the relationship between $T_e([O II])$ and Z_{Te} is shown for fixed values of $T_e([O III])$, $[O III]/H\beta$, and $[O II]/H\beta$ measured from a typical spaxel in SAMI609396B (see legend). The purple line shows oxygen abundance determined according to equations D3–D5 for various values of $T_e([O II])$, while the orange line shows Yates et al. (2020) metallicity-dependent fit to the $T_e([O II]) - T_e([O III])$ relation at a fixed value of $T_e([O III])$. The Y20 iterative method as originally outlined favours the lower branch solution (red circle). The Y20 correction increases the metallicity (green open circle), although not to the value of the upper branch. Both $Z_{Te, LS12}$ and $Z_{Te, SII}$ (refer to Section 4; $T_e([S II]) = 9500$ K) fall quite close to the upper branch solution (open blue circle and filled grey circle, respectively).

$[O III]/H\beta$ line ratios given values for $T_e([O II])$ and $T_e([O III])$:

$$O^+/H^+ = \frac{[O II]\lambda\lambda 3726, 29}{H\beta} g_1 \alpha_{H\beta} \sqrt{T_e([O II])} \times \exp[E_{12}/kT_e([O II])] \times \frac{\beta}{E_{12}\Upsilon_{12}}. \quad (D3)$$

$$O^{++}/H^+ = \frac{[O III]\lambda\lambda 4959, 5007}{H\beta} g_1 \alpha_{H\beta} \sqrt{T_e([O III])} \times \exp[E_{12}/kT_e([O III])] \times \frac{\beta}{E_{12}\Upsilon_{12}}. \quad (D4)$$

$$Z_{Te} \equiv 12 + \log(O^+/H^+ + O^{++}/H^+). \quad (D5)$$

The reader is referred to Yates et al. (2020) and Nicholls et al. (2014) for more details on these equations including the values and calculations of various parameters used.

D2 Two-valued solution of the Yates method

In Yates et al. (2020), the authors propose solving these equations with fixed point iteration, however we instead propose numerically solving for the intersection of equations (D1) and (D5). This preference is based on our observation that the relations described in

equations (D1) and (D5) in fact yield two solutions within the range of what could be considered physically reasonable.⁶

This is illustrated in Fig. D1 for an example typical SAMI609396B spaxel with $T_e([O III]) = 10^4$ K, and $[O III]/H\beta$ and $[O II]/H\beta$ line ratios of 3.54 and 2.42, respectively. For this example spaxel it can be seen that two possible solutions exist: (1) at $T_e([O II]) = 9342$ K and $Z_{Te} = 8.31$, and (2) at $T_e([O II]) = 14662$ K and $Z_{Te} = 8.03$. Neither of these solutions is physically implausible and while solution (1) would fall in a more densely populated region of the $T_e([O II]) - T_e([O III])$ relation as shown in Yates et al. (2020) (refer to fig. 5 in that paper), observed points comparable to solution (2) are found in their sample too.

Indeed, beyond the single example shown in Fig. D1, we find that all spaxels in SAMI609396B with at least one solution have precisely two. How then should we decide which of these two solutions to adopt?

The blue open circle in Fig. D1 shows that the $T_e([O II])$ obtained via the López-Sánchez et al. (2012) $T_e([O II]) - T_e([O III])$ relation (refer to equation 6 in Section 4.1) agrees quite well with the lower valued $T_e([O II])$ solution. However, this disregards the point of the Y20 method and findings presented in this work: that assuming a simple fixed relationship between $T_e([O II])$ and $T_e([O III])$ can be misleading.

The Y20 iterative method as originally applied in Yates et al. (2020) selects for the ‘lower branch’ (red circle in Fig. D1). However, subsequent application of the Y20 correction serves to shift this point to a slightly higher metallicity, partly toward the upper branch solution (green open circle in Fig. D1).

To investigate this further, the original Y20 sample was revisited with the two-valued solution in mind (Yates, private communication). It was found that targets where the direct⁷ metallicity was closer to the ‘upper branch’ solution were often targets with an O32 value below the threshold value for which the Y20 correction should be applied ($O32 \leq 0.29$). Thus, this O32 threshold could be used to distinguish between the lower and upper branches. All spaxels across the spatial extent of SAMI609396B fall in this category with $O32 \leq 0.29$ (refer to Fig. 8), meaning we would adopt the upper branch value under this scheme, rather than the lower branch value favoured by the original iterative implementation.

While we do not directly measure $T_e([O II])$, in Section 3.3 we derived $T_e([S II])$ from the $[S II]\lambda\lambda 4069, 76 / \lambda\lambda 6716, 31$ line ratio (refer to Fig. 4). Panel (e) of Fig. 4 shows that $T_e([S II]) < T_e([O III])$ across the majority of spaxels in SAMI609396B, with a median value of $T_e([S II]) = 9295$ K. Given that previous studies have found that $T_e([S II])$ and $T_e([O II])$ are often in general agreement (e.g. Croxall et al. 2016), we consider that this additionally supports our selection of the upper-branch value. We note, however, that large scatter is known to exist in both the $T_e([S II]) - T_e([O II])$ and $T_e([S II]) - T_e([O III])$ relations.

D3 Comparison between Yates method and LS12 method

In line with our methods outlined in Appendix D2 above, we consider two versions of the Y20 method: one in which we adopt the ‘upper branch’ solution to the Y20 method, and another where we adopt the

⁶More generally, it is possible that for some observations there will be no solution. In these cases, solving via the iterative method may be preferable (Yates, private communication).

⁷Here ‘direct’ metallicity refers to a metallicity in which both $T_e([O II])$ and $T_e([O III])$ have been directly measured with auroral lines.

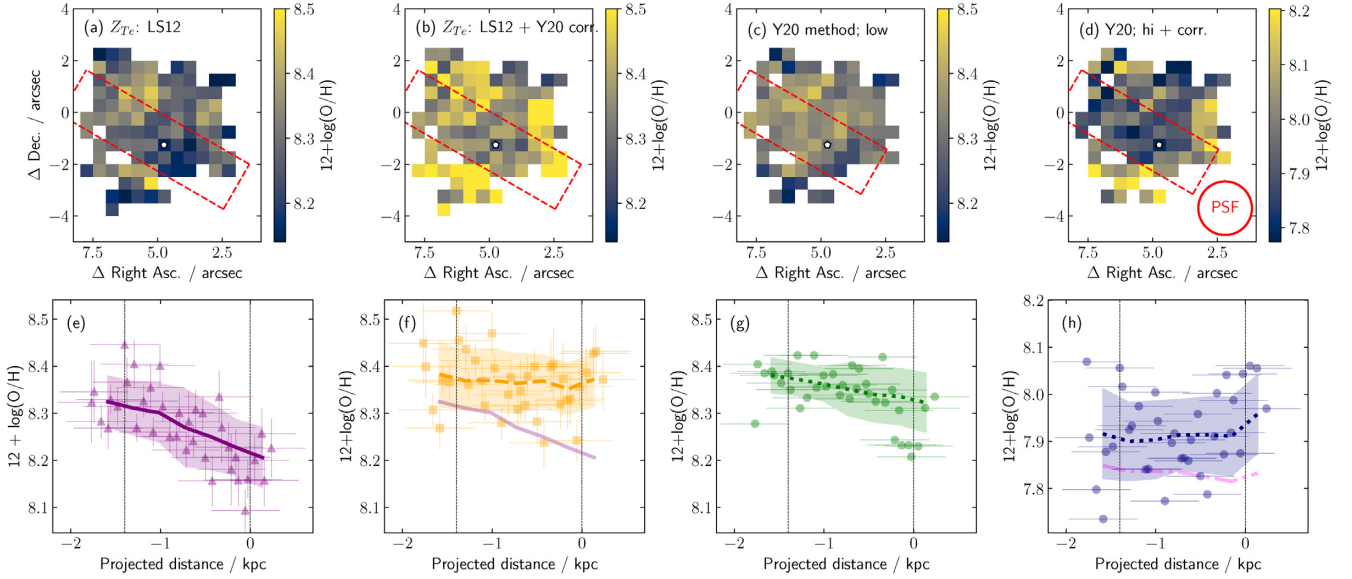


Figure D2. Comparison between the $Z_{Te, LS12}$ method described in Section 4.1 and the two solutions arising from the **Y20** method. Far left-hand and centre left-hand columns are simply reproduced from Fig. 5. The centre right-hand column shows the **Y20** upper branch metallicities, while the far right-hand column shows corrected **Y20** lower branch metallicities (the uncorrected lower branch metallicity trend is shown in panel h as the magenta dot-dashed line). Note: We do not take the step of propagating measurement errors through the **Y20** method. However, the input measurement uncertainties are from the same source as those in panels (e) and (f) and thus would likely be comparable.

‘lower branch’ and apply the **Y20** empirical correction. We find that the resulting $T_e([O II])$ and Z_{Te} maps are smooth with no unexpectedly large variations observed between pairs of adjacent spaxels.

In Fig. D2 we compare the metallicities obtained from these **Y20** methods with those obtained in Section 4.1 from the $Z_{Te, LS12}$ method. Metallicity maps and spatial trends in the far- and centre left-hand columns of Fig. D2 are simply reproduced from Fig. 5 and show the $Z_{Te, LS12}$ method with and without the **Y20** empirical correction. The centre right-hand column shows the **Y20** upper branch metallicities, while the far-right-hand column shows corrected **Y20** lower branch metallicities (additionally, the uncorrected lower branch metallicity trend is shown in panel h as the magenta dot-dashed line).

We first note that, even after the **Y20** correction, the lower branch metallicities are significantly lower than any of our other semidirect methods.⁸ The large scatter in the values obtained makes it difficult to determine the spatial metallicity trend from this method, however, qualitatively it does seem to be broadly consistent with the trend seen in the $Z_{Te, Y20}$ method applied in Section 4.1.2.

The normalization of the upper branch values is in much better agreement with other semidirect methods. The effect on the spatial trend is less clear: it appears somewhat flattened compared to $Z_{Te, LS12}$, however if a gradient were to be computed it would likely depend strongly on a cluster of lower metallicity points with projected distance $r \approx 0$ kpc.

Yates et al. (2020) showed that the semidirect abundance deficit at low O^{++}/O^+ (which the **Y20** correction aims to address) is present across all $T_e([O II]) - T_e([O III])$ relations considered in that work,

including LS12 (fig. 6 in Yates et al. 2020). In particular, they show in detail its effect on the **Y20** lower branch metallicities. Although it seems that low O^{++}/O^+ values seem to correlate with an increased preference for the upper branch metallicity solution, it is currently unclear whether variations in O^{++}/O^+ result in semidirect metallicity biases in a similar way to that observed by Yates et al. (2020) with respect to the lower branch solution and other $T_e([O II]) - T_e([O III])$ relations. In the context of SAMI609396B where we have shown large scale variations in the $[O III]/[O II]$ ratio, the existence of such a bias could affect our interpretation of the spatial metallicity trend resulting from this upper branch solution. Addressing this issue would require a more detailed analysis of a more extensive sample (e.g. the Yates et al. (2020) sample) and is beyond the scope of this paper.

In summary, we find that the **Y20** semidirect method as originally proposed favours a similar spatial gradient to that of $Z_{Te, Y20}$ after the application of the **Y20** correction, albeit at a much lower normalization. After identifying the two-valued nature of these relations, we found that adopting the upper branch values resulted in normalization that agreed much better with other methods. We defer commenting on the spatial trend arising from these upper branch values to a later study, after the two-valued nature of the **Y20** relations has been examined in more detail.

Overall, these findings do not alter the main conclusion of this work: that assumptions around the temperature structure of H II regions can have a significant impact on measured spatial metallicity trends in IFU observations of galaxies.

⁸And, indeed, strong-line methods; although some degree of offset is expected there (e.g. Kewley & Ellison 2008)